Porous thermosensitive coating with water-locking ability for enhanced osteogenic and antibacterial abilities

Xueqing Hao [a],[1], Jielong Zhou [b],[1], Juning Xie [b], Xianrui Zou [a], Baoe Li [a], Chunyong Liang [a],[d],**, Yu Zhang [b], Feng Peng [b],***, Donghui Wang [c],*

[a] School of Materials Science and Engineering, Hebei University of Technology, Tianjin, 300130, China
[b] Medical Research Center, Department of Orthopedics, Guangdong Provincial People's Hospital, Guangdong Academy of Medical Sciences, Guangzhou, Guangdong, 510080, China
[c] School of Health Sciences and Biomedical Engineering, Hebei University of Technology, Tianjin, 300130, China
[d] Fujian Provincial Key Laboratory for Advanced Micro-nano Photonics Technology and Devices, Research Center for Photonics Technology, Quanzhou Normal University, China

ARTICLE INFO

ABSTRACT

Preferable antibacterial property and osteogenesis are the permanent pursuit for metallic implants. However, it is difficult to satisfy both the properties. In fact, implants may be contaminated with bacteria during storage and surgery, leading to inflammation. Therefore, the antibacterial property of biomaterial surfaces is required not only in the human environment but also at room temperature. In this study, porous structures loaded with a thermosensitive poly (N-isopropylacrylamide) (PNIPAM) hydrogel on a nitinol (NiTi) substrate were constructed. When the temperature is 25 °C, almost all bacteria cannot adhere to the sample surface due to the abundant hydration layer of the PNIPAM hydrogel. Meanwhile, when the temperature is 37 °C, the structure of the PNIPAM hydrogel collapses and the hydration layer disappears due to the temperature change. However, the porous structures lock water in the pores, which results in a high-hydration-rate sample surface. This surface has few bacterial adhesion sites; nevertheless, the adhesion of larger cells to the surface is not impeded by the porous structure. In addition, the PNIPAM hydrogel is soft and biocompatible, so the sample can have better cell adhesion and proliferation than a bare NiTi alloy. Based on these results, it can be concluded that the porous NiTi sample loaded with the thermosensitive PNIPAM hydrogel has the antibacterial property before implantation and the dual function of inhibiting bacterial adhesion and promoting cell adhesion and proliferation after implantation, which shows promising applications in the biomedical field such as orthopedic implantation.

1. Introduction

Titanium-based implantable devices have been widely used in the dental, orthopedic and intracavitary fields due to their excellent chemical stability, mechanical properties, and biocompatibility [1,2]. However, in clinical application, the presence of metallic implants will induce foreign body reaction and impair the immune system around the implants, causing bacteria to colonize [3]. Unfortunately, titanium and titanium alloys lack antibacterial ability, and bacterial infection has become a serious complication that leads to implant failure [4–6].

Numerous surface modification methods have been proposed to

provide implants with antibiosis ability. The most used strategy to combat bacterial infections is using antibiotics or transition metal ions (such as silver, copper, and zinc) [7]. However, it may cause drug resistance [8] and cytotoxicity [9,10], and implants may still undergo bacterial infection after the antibiotics is completely released. Therefore, this strategy cannot work for a long time [11]. To provide implants with long-term antimicrobial ability, researchers permanently immobilize bactericidal agents like quaternary ammonium salts [12], quaternary phosphonium groups [13], antibacterial peptides [14], lysozymes [15], and chitosan derivatives [16] on the implant surface. Unfortunately, the aforementioned implants only kill bacteria that adhered to the sample

---

surface, and the continued deposition of dead bacteria and debris on the surface can significantly reduce their bactericidal performance [17,18]. A number of materials such as hydrogels or zwitterionic polymers [19] have been reported to possess antifouling ability, which gives inspiration to the scientists to construct antifouling coatings on the surface of the implants, that directly inhibit bacterial adhesion. Due to their high efficiency in combating bacterial attachment and their high biocompatibility, antifouling coatings show great potential to be used in implant modification. However, cells are unable to adhere to the antifouling surface either, thus limiting their application in orthopedic implants, which require good cell adhesion for bone integration [20].

The need for antibacterial property of implanted devices is time dependent. Bacterial contamination is most likely to occur during preoperative storage and surgery. Thereafter, the host immune system lowers the infection risk [21–23]. Therefore, it is particularly important for the implanted devices to inhibit bacterial adhesion before entering the body. Considering that the temperature of a human body is maintained at around 37 °C, whereas the operating temperature is generally between 22 °C and 24 °C, the change in temperature can be regarded as a sign of the change in antibacterial demand. Therefore, the construction of temperature-sensitive coatings on material surfaces has become the focus of research. Different types of thermosensitive materials have been developed and used in the surface modification of implants; among them, PNIPAM hydrogel has attracted great attention due to its high biocompatibility and temperature-dependent antifouling ability [24]. When the environmental temperature is below the low critical solution temperature (LCST) (approximately 32 °C) of PNIPAM, its hydrophilic groups are exposed outside, resulting in the formation of a hydration layer, which resists bacterial attachment with high efficiency. On the other hand, after implanting into the body, when the temperature is above the LCST, the hydrophobic groups of PNIPAM are exposed, and the antifouling hydration layer disappears [25]. Therefore, the PNIPAM coating does not affect cell adhesion when implanted *in vivo*, but it still losses its preferable bacteria-resistant ability. Obtaining an implant surface with selective bacterial inhibition ability is of great interest but still under challenge.

Inspired by the fact that the good antifouling ability of PNIPAM below the LCST results from the formation of the hydration layer, this study designed a structure that maintains the good cell affinity of PNIPAM while effectively inhibiting bacterial adhesion at body temperature by grafting the PNIPAM hydrogel on a porous surface. NiTi, a widely used biomedical titanium-based alloy, was chosen as a substrate, a nanoscale pore layer was constructed on the surface of the NiTi alloy by electrochemical treatment, and the PNIPAM hydrogel coating was loaded on the surface of the structure by chemical binding [Scheme 1(a)]. The constructed nanostructures possessed the ability to "lock" water when immersed in a physiological environment, generating an artificial hydration layer with only few hydrophobic contact sites exposing outside [Scheme 1(b)]. When compared with a flat sample surface, the contact area between the bacteria and samples was greatly reduced, which provided the constructed samples with antibacterial property. The cell size is much larger than the pore size of the structure, so cell adhesion is not affected. In addition, the porous structures slightly reduced the surface modulus and the hardness of the implant, which were more favorable for osteogenesis.

2. Material and methods

2.1. Sample preparation

The NiTi sample used in the experiment has two shapes: the size of NiTi sample for *in vivo* osteogenesis experiment is Φ 2 mm × 8 mm, and the size of NiTi sample for other experiments is Φ 10 mm × 1 mm. The NiTi sample was ultrasonically cleaned with acetone, ethanol, and deionized water, soaked in a pickling solution [HF (35%):HNO$_3$ (68%):H$_2$O = 1:5:34] for 30 min twice, and then thoroughly rinsed with deionized water thrice. Cleaned NiTi was subjected to electrochemical

treatment at 25 °C in a conventional two-electrode electrochemical cell, which consisted of a NiTi electrode as the working electrode and graphite as the counter electrode, in a 2-M HNO$_3$ aqueous solution at 5 V for 10 min. After electrochemical treatment, the samples were cleaned and dried at 25 °C and denoted as "TiNL."

The PNIPAM hydrogel was constructed on the NiTi and TiNL samples through the following steps: The samples were placed into a muffle furnace (SX-G16103, China) and heated in air to 450 °C (heating rate: 5 °C/min) for 1 h. Thereafter, the samples were immersed in 2-M NaOH (Machlin, China) for 20 min. 3-(2-Bromoisobutyramido)propyl (triethoxy)-silane (BiBAPTES) can be synthesized as follows: In an inert nitrogen atmosphere, (3-aminopropyl)triethoxysilane (4.7 mL) (Rhawm, China) and α-bromoisobutyryl bromide (3.15 mL) (Rhawm, China) were sequentially added to a mixed solution of tetrahydrofuran (THF)/triethylamine (25 mL/4 mL) (Aladdin, China) at 0 °C with constant stirring. Thereafter, the mixture was heated to room temperature and stirred for 12 h. The residual THF solvent was evaporated under vacuum. The samples were completely immersed in a 4-vol% BiBAPTES ethanol solution (China National Medicines, China) for 45 min in air at room temperature. Each sample was washed with ethanol twice to remove excess BiBAPTES and dried under a stream of nitrogen gas. Surface-initiated atom transfer radical polymerization of NIPAM (Rhawm, China) was carried out by immersing the samples in a monomer solution consisting of 10% w/v NIPAM, 0.5% w/v CuBr (Rhawm, China), 0.1% w/v CuBr$_2$ (Rhawm, China), and 1.5% v/v Pentamethyldiethylenetriamine (Aladdin, China) in deionized water under a nitrogen atmosphere [26]. The reactions were generally performed at 25 °C for 12 min. The samples were rinsed thoroughly with deionized water after the reaction and dried under a stream of nitrogen gas. The PNIPAM-coated NiTi and TiNL samples were denoted as "PNIPAM/NiTi" and "PNIPAM/TiNL," respectively.

2.2. Sample characterization

The surface and cross-sectional morphology of the samples were examined by scanning electron microscopy (SEM) (JSM-7100F, Japan). The surface roughness was measured by atomic force microscopy (AFM) (A5500, USA). The crystal structure was investigated by X-ray diffraction (XRD) (D8 Discover, Germany) using Cu Kα radiation. The functional groups and the valence states of the elements in the sample surfaces were analyzed by Fourier-transform infrared spectroscopy (FT-IR) (Invenio-S, Germany) and X-ray photoelectron spectroscopy (XPS) (Escalab 250Xi, Germany).

2.3. Surface modulus and hardness of the sample

A nanometer indentation instrument (Anton Paar NHT³, Switzerland) was used to measure the surface hardness and elastic modulus. Five points were randomly tested to calculate the average.

2.4. Surface wettability test

The static water and oil (1,2-dichloroethane) contact angles in the air and in the water system of the different samples were measured at 25 °C and 37 °C, respectively. For measurements at 25 °C, 1.5-μL deionized water was dropped vertically on the dry sample surfaces in the air, and 1.5-μL oil droplets were dropped vertically on the sample surfaces submerged in the water system. The water contact angle (WCA) and the oil contact angle (OCA) were measured by a contact angle meter (JC2000, China). For measurements at 37 °C, the samples were heated to 37 °C or placed in the water that was heated to 37 °C with a heating agitator. Thereafter, the water or oil droplets were vertically dropped on the surface of the samples, and the images were captured. The JC2000 software was used to analyze the contact angles.
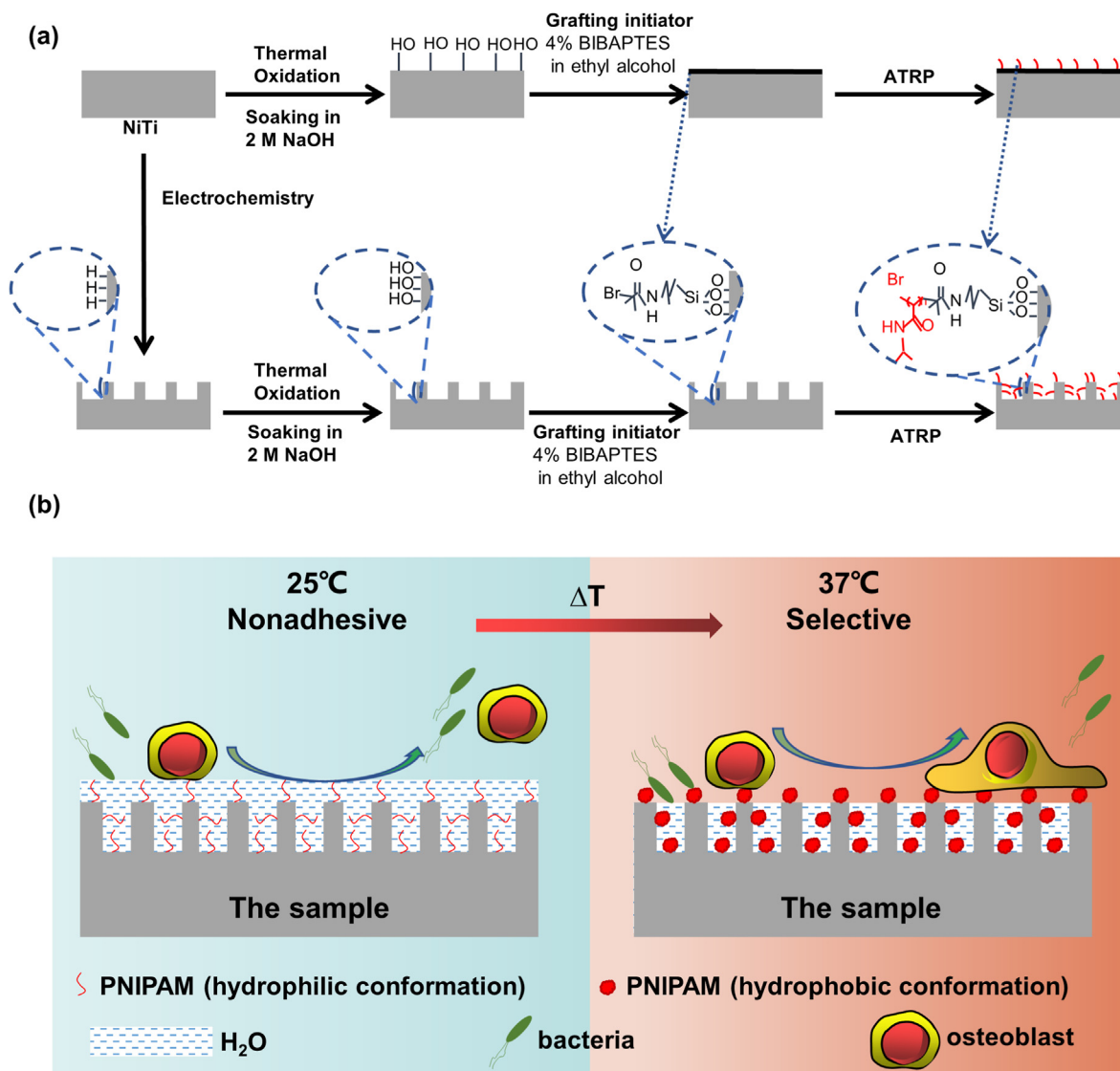
Scheme 1. (a) Loading of the thermosensitive PNIPAM hydrogel on the NiTi substrate; (b) Schematic diagram of the bacterial and cellular selective adhesion of the sample at 25 °C and 37 °C: At 25 °C, there is a hydration layer on the sample surface, which repels both bacteria and cells; on the other hand, at 37 °C, the structure of PNIPAM collapses and the surface no longer contains a hydration layer, but the nanoporous structure still retains water, reducing the number of bacterial adhesion sites. Meanwhile, for larger cells, this apparently no longer works.

2.5. Bacterial experiment

2.5.1. Bacterial live/dead staining

Escherichia coli (CMCC (B) 44,102) and *Staphylococcus aureus* (ATCC 6538) were selected as representative species, as they have the cell wall characteristics of Gram-negative and Gram-positive bacteria, respectively. Both bacteria were cultured in an LB medium at 37 °C. A 1-L LB medium contained 10-g tryptone (Oxoid, U.K.), 3-g beef extract powder (Hopebio, China), and 5-g NaCl (China National Medicines, China). The pH of the media was adjusted to 7.2. The absorbance values of different bacterial solutions at 600 nm wavelength were measured by an enzyme-labeled instrument (DNM-9602, China). After gradient dilution, the bacterial solution was evenly spread on the agar plate, and the bacterial concentration corresponding to the absorbance value was determined by counting the number of colonies. According to the results of multiple groups, the regression equation was obtained, and it was determined that when the absorbance of the bacterial solution was 0.1, the corresponding bacterial concentration was 10^7 CFU/mL. Select the bacterial concentration as 10^6 CFU/mL for bacterial experiments *in vitro*.

The integrity of the bacterial cell membrane and the live/dead state

were stained with fluorescent reagent by bacterial live/dead staining (LIVE/DEAD BacLight Bacterial Viability Kit, L13152, molecular probes). An 80-μL bacterial suspension (10^6 CFU/mL) was dropped onto the surface of the samples, and the samples were then placed into a constant-temperature incubator at 25 °C and 37 °C for 12 h. Thereafter, each sample was cleaned with phosphate buffer solution (PBS) twice, 500 μL of fluorescent dye was then added to each sample well, the dye was sucked after standing for 15 min in the dark, and the free dye was cleaned with PBS thrice. The survival status of the bacteria was observed by a laser scanning confocal microscope (Leica SP8, Germany).

2.5.2. Agar plate coating test

An 80-μL bacterial suspension was dropped on the surface of the samples, and both bacteria were adjusted to 10^6 CFU/mL and cultured for 12 h at 25 °C and 37 °C, respectively. The samples were cleaned with PBS twice to remove the bacteria that did not adhere to the sample surface. Thereafter, the sample was immersed in 4-mL PBS and shaken for 30 s to separate the adhered bacteria, and then 100-μL of the obtained bacterial suspension was inoculated onto LB agar plates and spread evenly with sterile glass rods. The culture plate coated with bacteria was

placed in an incubator at 37 °C for further culture for 16 h and then photographed for observation.

2.5.3. Bacterial micromorphology

The bacteria (10^6 CFU/mL, 80 μL) were inoculated and cultured on the surface of the samples for 12 h at 25 °C and 37 °C. The samples were cleaned with PBS twice; then, 1-mL 2.5% glutaraldehyde (Solarbio, China) was added for fixation. After storing at 4 °C overnight, the samples were dehydrated with ethanol having volume fractions of 30%, 50%, 70%, 75%, 80%, 85%, 90%, 95%, and 100% for 10 min each, followed by the mixed solutions of ethanol and hexamethyldisilazane (HMDS) (Solarbio, China) in different proportions (ethanol:HMDS = 2:1, 1:1, 1:2, 0:1). Thereafter, the samples were sprayed with gold and observed using SEM.

2.6. Subcutaneous implantation

To evaluate the anti-infection ability of the PNIPAM/TiNL sample *in vivo*, mice infected with *E. coli* were used as the anti-infection model. The animal experiment was conducted in accordance with the principles of the Animal Experiment Ethics Committee of Nankai Hospital. 24 male BALB/c mice were divided into four groups and implanted with the NiTi, TiNL, PNIPAM/NiTi, and PNIPAM/TiNL samples, respectively. During the operation, a wound of about 10 mm was cut on the back of each mouse, and a sample containing 80-μL 10^4-CFU/mL *E. coli* was implanted subcutaneously. It was worth noting that the surface of the samples attached by the bacteria should be in contact with the mouse endodermis. The mice were sacrificed three days after implantation, and the samples and surrounding tissues were collected. The samples and tissues were fixed in 4% paraformaldehyde (PFA) (Shanghai Yuanye Bio-Technology Co, Ltd, China). After the samples were dehydrated and fixed in gradient ethanol solution according to the above method, the number and the morphology of *E. coli* on the surface of the samples were observed using SEM. At the same time, after paraffin embedding, conventional tissue sections were made and stained by hematoxylin and eosin staining (HE, Solarbio, China), as well as Masson's trichrome staining (MASSON, Solarbio, China) and observed by an optical microscope (XD-202, China). The Image J software was used to analyze the images to obtain the density of inflammation-related cells.

2.7. Cell experiment

2.7.1. Cell adhesion

Rat bone marrow mesenchymal stem cells (rBMSCs) (Stem cell bank, Chinese Academy of Science, China) were cultured in alpha Minimum Essential Medium (Gibco BRL, USA) containing 10% fetal bovine serum (FBS, Hycione, USA), 100-U/mL streptomycin, and 100-U/mL penicillin. Human umbilical vein endothelial cells (HUVECs) (Stem cell bank, Chinese Academy of Science, China) were cultured in Endothelial Cell Growth Medium (Gibco BRL, USA). The culture media were refreshed every 2 days, and when the cell fusion rate reached 80%–90%, the subculture was carried out. Third generation of the cells was selected for the experiment. The concentration of cells was measured by the Cell Counter (C100, China).

The samples were exposed to a UV lamp for 4 h to sterilize. The rBMSCs (5×10^4 cells/mL) were seeded onto the surface of the samples and cultured for 1, 6, and 24 h at 37 °C. The samples were then rinsed with PBS and fixed in 4% PFA. A 0.1% v/v Triton X-100 surfactant (Sigma-Aldrich, USA) was added to permeate the cells. Thereafter, the cells on the samples were blocked in 1-wt% bovine serum protein (BSA, Sigma, USA). Thereafter, the cells were stained with phalloidin (Sigma-Aldrich, USA) and 4,6-diamidino-2-phenylindole (Sigma-Aldrich, USA) and observed through fluorescence microscopy (IX 71, Olympus, Japan). The initial adhesion of HUVECs on the surface of the samples was observed according to the procedures described above.

2.7.2. Cell proliferation

The rBMSCs were inoculated on the sample surface at a density of 5×10^4 cells/mL. After 1, 4, and 7 days of culture, Cell Counting Kit 8 (CCK-8) (Solarbio, China) was used to evaluate cell proliferation according to the manufacturer's instruction. The HUVECs were inoculated on the sample surface at a density of 1×10^4 cells/mL. After 1 day of culture, cell proliferation on the sample surface was observed by the assays described above.

2.7.3. Cell live/dead staining

The rBMSCs (5×10^4 cells/mL) were inoculated on the surface of the samples and cultured for 4 days. Thereafter, 500 μL of mixed calcein AM and propidium iodide staining reagent (Thermo Fisher Scientific, USA) was used to stain the cells. After rinsing with PBS, the cells were observed using fluorescence microscopy. The HUVECs were inoculated on the surfaces at a density of 1×10^4 cells/mL and cultured for 1 day. The condition of HUVECs on the surface of the samples was observed according to the procedures described above.

2.7.4. Characterization of extracellular matrix (ECM) mineralization

The rBMSCs [5×10^4 cells/mL (7 days) and 3×10^4 cells/mL (14 days)] were seeded on the surface of the samples. After 8 h of cultivation, an osteogenesis induction medium supplemented with 10^{-2}-M β-sodium glycerophosphate, 50-μg·mL^{-1} L-ascorbic acid, and 10^{-7}-M dexamethasone was added to induce osteogenesis. The osteogenesis induction medium was changed every 3 days. At 7 and 14 days, the cells were fixed with 70% ethanol and then stained with 40-mM alizarin red (ARS, Sigma-Aldrich, USA, with pH = 4.2). The cells were observed by optical microscopy. For the quantitative experiments, 10% cetylpyridinium chloride elution (Aladdin, USA) was used to dissolve the dye, and the absorbance at 620 nm of the extract was measured by an enzyme-labeled instrument.

2.7.5. Alkaline phosphatase (ALP) activity assay

The rBMSCs were cultured as mentioned in section 2.7.4. The cells were lysed in RIPA (P0013B, Beyotime) on the ice and then centrifuged at 12,000 g at 4 °C, and the supernatant was maintained. The total ALP activity was detected by the ALP Detection Kit (P0321S, Beyotime). The results were normalized to the total intracellular protein content calculated using a bicinchoninic acid kit (Thermo Fisher Scientific, USA).

2.7.6. Real-time polymerase chain reaction (RT-PCR) analysis

The rBMSCs were cultured as mentioned in section 2.7.4. Thereafter, the cells were lysed and ribose nucleic acid (RNA) was extracted using Total RNA Kit I (R6834-01, Omega). Complementary deoxyribonucleic acid (cDNA) was further synthesized and RT-PCR was performed on a Light Cycler480 system (Roche, Switzerland). The primer sequences of the detected genes are listed in Table S1.

2.7.7. Fluorescence expression of CD31

The HUVECs were cultured on the surface of the samples for 4 days (5×10^4 cells/mL) and 7 days (3×10^4 cells/mL). Thereafter, the cells were isolated and suspended by a flow cytometry staining buffer (00-4222-26, Thermo Fisher Scientific, USA). After blockage, FITC-CD31 labeled mouse antihuman monoclonal antibody was added. After rinsing twice, flow cytometry analysis was performed (FCM, EPICS Profile II, Coulter, USA).

2.7.8. Angiogenic evaluation of HUVECs in vitro

After being thawed at 4 °C, 300 μL of Matrigel (BD Matrigel 356,234, USA) was coated into precooled 24-well culture plates per well. The plates were placed into the incubator to allow the gelling of Matrigel. Thereafter, 1 mL of HUVEC suspension (1.8×10^4 cells/mL) was added into each well. After 4 h of culture, the culture medium was replaced by extracts (obtained by immersing each specimen in 1 mL of culture for 24 h). After being cultured for another 12 h, the formed tube structures were

observed and imaged under a phase contrast inverted microscope (Olympus, Germany).

2.8. In vivo osseointegration evaluation

A total of 24 male rats (Sprague Dawley) were used in this study. The animal experiment was conducted in accordance with the principles of the Animal Experiment Ethics Committee of Nankai Hospital and the international standards on animal welfare. A hole (2 mm in diameter) was drilled into the distal surface of the femoral condyles. After implantation of the columnar samples for 8 and 12 weeks, the rats were sacrificed, and the femurs were collected and fixed in formalin. The femurs were scanned using micro computed tomography (Micro-CT) (Viva CT40, SCANCO Medical AG), and the three-dimensional (3D) image of each sample was reconstructed using the Inveon Image Research Workplace (Siemens, Germany). The bone volume percentage (BV/TV), trabecular number (Tb·Th), and bone mineral density (BMD) were analyzed. After Micro-CT scanning, the femur specimens were dehydrated with ethanol, embedded in polymethyl methacrylate, and cut into sections by a saw microtome (EXAKT Apparatebau, Germany). The sections were stained with Van Gieson's stain and imaged through a stereoscopic microscope.

2.9. Statistical analysis

All data are presented as the mean ± standard deviation (SD).

Statistical comparisons were conducted with ANOVA followed by Tukey's test for multiple comparisons. All statistical analyses were performed using Prism statistical software (GraphPad Software, CA, USA). The difference with $p < 0.05$ was considered to be significant and marked as "*," that with $p < 0.01$ was marked as "**," that with $p < 0.001$ was marked as "***," and that with $p < 0.0001$ was marked as "****."

3. Results and discussion

3.1. Construction and characterization of porous layers coated with PNIPAM hydrogel

Porous structures were constructed on the surface of a NiTi alloy by electrochemical etching. As shown in Figure S1, discontinuous porous structures were formed. The coverage ratio of the porous structures increased with the applied voltage and reaction time until the applied voltage reached 5 V and the reaction time was prolonged to 10 min. By continuing to increase the voltage or prolong the reaction time, the coverage ratio of the porous structures did not change much. Therefore, an applied voltage of 5 V and a reaction time of 10 min were determined to be the best process parameters and used in the following experiment. The formation mechanism of the porous structures was discussed in detail in the supporting information (Note S1).

Fig. 1(a) showed the SEM images of the NiTi, TiNL, PNIPAM/NiTi, and PNIPAM/TiNL samples. The surfaces of the NiTi and PNIPAM/NiTi samples were relatively smooth with only a few bumps and lumps, which
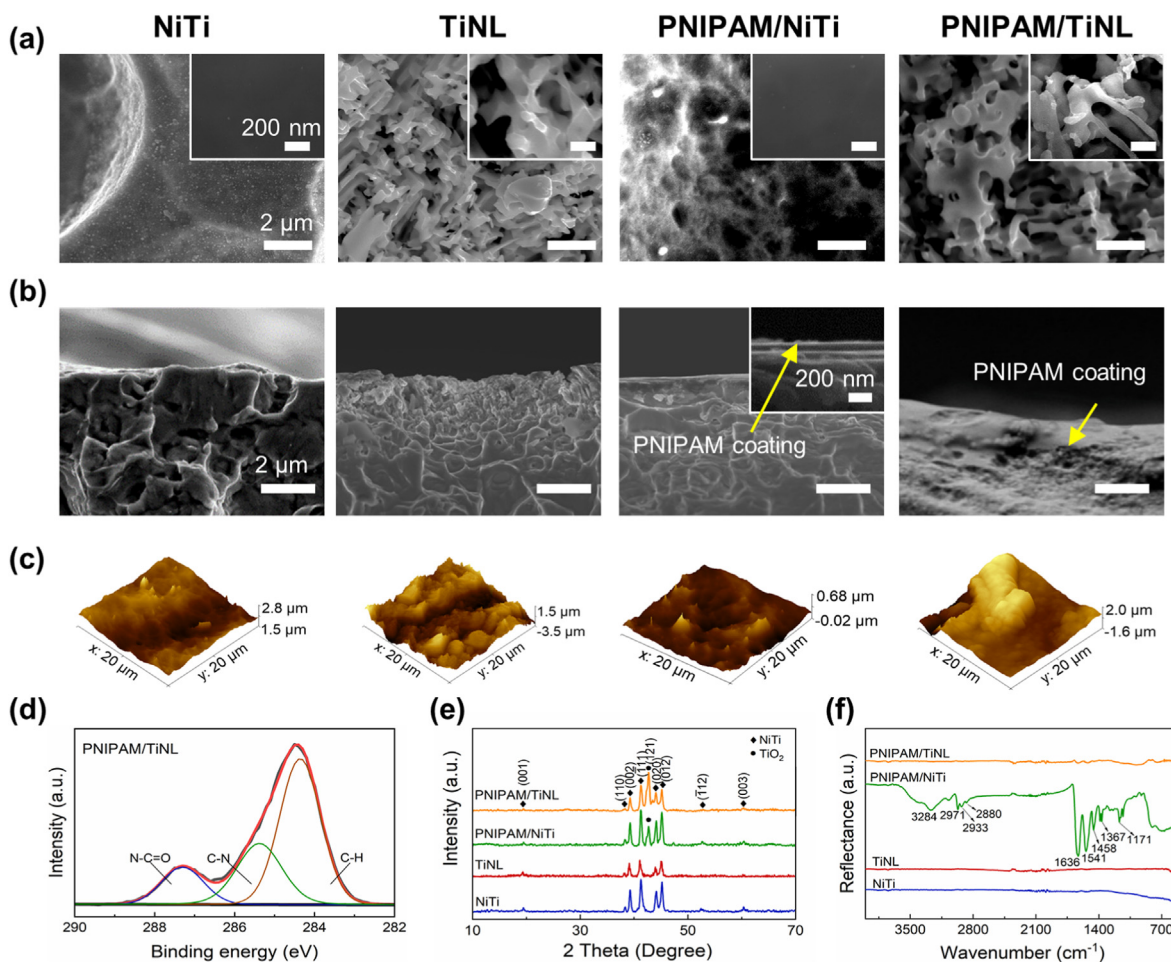

Fig. 1. (a) SEM images of the NiTi, TiNL, PNIPAM/NiTi, and PNIPAM/TiNL samples; (b) SEM images of the cross sections of the NiTi, TiNL, PNIPAM/NiTi, and PNIPAM/TiNL samples; (c) AFM of the NiTi, TiNL, PNIPAM/NiTi, and PNIPAM/TiNL samples; (d) C 1s core-level spectrum of the PNIPAM/TiNL sample surface, which could be curve-fitted with three peak components (C–H, C–N, and N–C═O) with binding energies; (e) XRD patterns; and (f) FT-IR spectra of the NiTi, TiNL, PNIPAM/NiTi, and PNIPAM/TiNL samples.

resulted from the pickling pretreatment. The TiNL and PNIPAM/TiNL samples prepared by electrochemical etching presented porous structures on the surface with pore sizes of about 370–450 nm. The cross-sectional images [Fig. 1(b)] showed that the thickness of the porous layer was about 4 μm. In addition, it could be seen from the cross-sectional view that the PNIPAM hydrogel coating (the yellow arrow indicated) was evenly spread on the sample surface, and its thickness was in the range of 30–100 nm. The surface became coarser after the electrochemical processing. The AFM test [Fig. 1(c)] showed that the roughness (Rms) of the NiTi sample increased from 170.2 to 802.0 nm after electrochemical treatment. The loading of the PNIPAM hydrogel reduced the surface roughness to a certain extent, and the surface roughness of the PNIPAM/NiTi and PNIPAM/TiNL samples were 66.91 and 659.2 nm, respectively.

The XPS spectrum showed that Ni, Ti, O, and C existed on the surface of the NiTi sample [Figure S2(a)]. On the surface of the TiNL sample, the peak of Ni disappeared because of the selective Ni etching in the electrochemical reaction, which was in accordance with a previous report [27,28]. Only C, N, and O, which are the characteristic elements in PNIPAM, could be detected on the surface of the PNIPAM/NiTi and PNIPAM/TiNL samples, this is because the sampling depth of XPS is about 2–5 nm, and the PNIPAM is detected on the surface of the sample loaded with PNIPAM hydrogel. Therefore, the relative content of Ti and Ni decreased, and correspondingly, the characteristic element C, N and O of PNIPAM increased. It suggested the successful loading of the PNIPAM hydrogel. The Ti 2p core-level spectrum of the NiTi and TiNL samples [Figure S2(b)] could be fitted for two peak components with binding energies of 464.3 and 458.6 eV, corresponding to the binding energy of Ti^{4+} in TiO_2, which indicated that Ti existed mainly in the form of TiO_2 on the surface of the NiTi and TiNL samples. The Ti signal on the other two samples was very weak, and the existence of Ti could hardly be detected; at the same time, the relative content of C increased. The C 1s core-level spectrum of the PNIPAM/TiNL sample surface was further analyzed [Fig. 1(d)]. The curve could be divided into three peaks with binding energies of 284.8, 285.5, and 288.0 eV, which are attributable to the C–H, C–N, and N–C=O species, which are the functional groups of PNIPAM [29,30]. The XPS results proved that the porous structure formed by electrochemistry was TiO_2 and the PNIPAM polymer was successfully loaded on the sample surface.

Fig. 1(e) showed the XRD patterns of the different samples. Only the peaks corresponding to NiTi (PDF#35–1281) could be detected from the NiTi and TiNL samples, and an obvious peak corresponding to the (1 2 1) crystal plane of TiO_2 appeared in the XRD patterns of the samples loaded with PNIPAM hydrogel. The presence of TiO_2 on the NiTi and TiNL samples could not be detected by XRD, which might result from the oxide film formed that was relatively thin. The X-ray directly penetrated the oxide film and reached the NiTi substrate. With regard to the PNIPAM-hydrogel-coated samples, they were heated to 450 °C for thermal oxidation in a muffle furnace during the loading of PNIPAM, which increased the thickness of the oxide layer. Therefore, TiO_2 could be easily

detected from the PNIPAM-coated samples by XRD. It should be noted that the characteristic peak of TiO_2 on the surface of PNIPAM/TiNL was stronger than that of PNIPAM/NiTi, verifying that the major crystal phase of the porous structure layer obtained by electrochemical treatment was TiO_2, which increased the content of TiO_2 compared with the PNIPAM/NiTi sample. No amorphous diffraction peak of the PNIPAM polymer was detected by XRD, because the thickness of the PNIPAM polymer coating was less than 100 nm, which was too thin to be detected by XRD.

FT-IR was performed and its spectra were presented in Fig. 1(f). No peaks were detected on the surface of the NiTi, TiNL, and PNIPAM/TiNL samples. The result of the PNIPAM/NiTi sample showed peaks at 1636 cm^{-1} corresponding to the stretching vibration absorption peak of C=O in the PNIPAM polymer, at 1541 cm^{-1} corresponding to the C–N–H bending vibration absorption peak, at 3284 cm^{-1} corresponding to the N–H stretching vibration absorption peak of the amide group, and at 1458 cm^{-1} corresponding to the antisymmetric bending vibration absorption peak of –CH_3 and the symmetric bending vibration absorption peak of –CH_2, and it showed a group of three peaks between 2800 and 3000 cm^{-1} which were assigned to C–H stretching vibrations. In addition, the interaction between the C–H stretching and bending vibration of the isopropyl group produced two splitting peaks with similar strength at 1387 and 1367 cm^{-1}, which confirmed the existence of the isopropyl group [31–33]. The appearance of these peaks provided strong evidence for the successful loading of PNIPAM onto the substrate surface. However, due to the implementation of electrochemical treatment, the roughness of the sample surface was greatly increased, and infrared light could not reflect the information back to the sample surface due to diffuse reflection, resulting in that nearly no FT-IR peaks could be detected from the PNIPAM/TiNL samples. FT-IR is a molecular absorption spectrum, while the NiTi and TiNL samples are atomic structures, and infrared light cannot cause metal atoms to vibrate or rotate. Therefore, there are no FT-IR peaks for the NiTi and TiNL samples. In general, it can be concluded from the above results that the TiO_2 nanoporous structures have been successfully constructed, and the PNIPAM hydrogel was effectively coated on the structures.

3.2. Surface modulus and hardness of the PNIPAM/TiNL sample

The surface of materials is the place where materials communicate with cells, and its physical and chemical properties determine its biological properties. When a medical material is implanted into the human body as a force part, its mechanical properties must have a good match with the human bone [34]. Therefore, it is very necessary to test the surface mechanical properties of the samples. Fig. 2(a) presented the nanoindentation load–displacement curves for various samples at a load of 200 mN. Under the same load condition, the corresponding curves of the TiNL and PNIPAM/TiNL samples were more to the right, indicating that they could achieve larger displacement and the surface was more
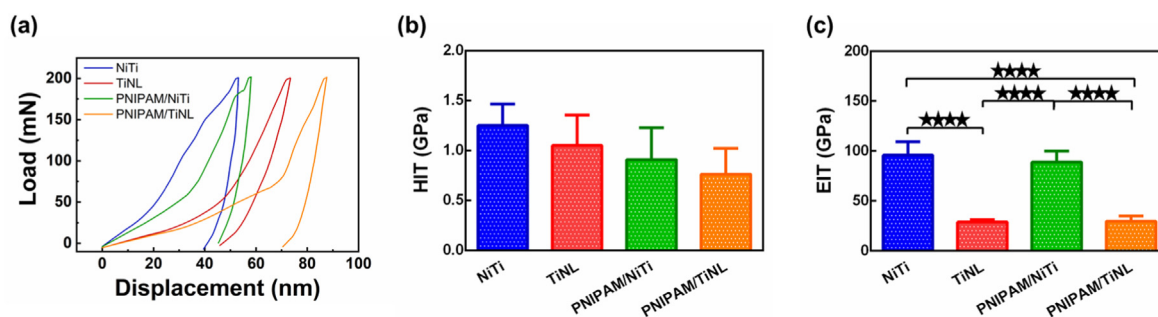

Fig. 2. (a) Load–displacement curves, (b) hardness values, and (c) elastic moduli of the NiTi, TiNL, PNIPAM/NiTi, and PNIPAM/TiNL samples. One-way ANOVA with Tukey's multiple comparisons test was used to test the difference in hardness values and elastic moduli. There is no statistical difference in Fig. 2(b). **** indicates p < 0.0001.
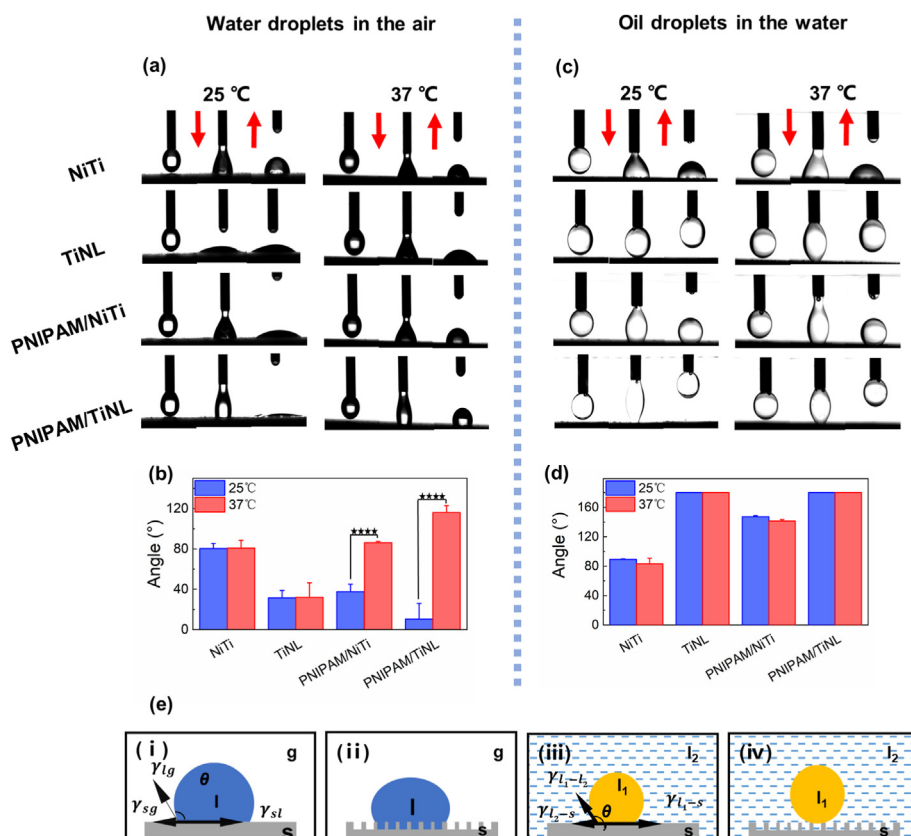
Fig. 3. (a) CA images of the water droplets and (b) the numerical statistics on the NiTi, TiNL, PNIPAM/ NiTi, and PNIPAM/TiNL surfaces in the air. (c) CA images of the oil droplets (1,2-dichloroethane) and (d) the numerical statistics on the NiTi, TiNL, PNI-PAM/NiTi, and PNIPAM/TiNL surfaces in the water. (e) Effect of surface structure on the wetting behavior of solid substrates in solid/oil/water three-phase systems: (i) diagram of Young's equation of a water droplet in a gas–liquid–solid three-phase system; (ii) Cassie's model describing the contact angle at a rough surface in the air; (iii) diagram of Young's equation at the condition of a liquid 1 droplet on a smooth surface in a liquid 2 phase; (iv) Cassie's model describing the contact angle at the condition of a liquid 1 droplet on a rough surface in a liquid 2 phase. Two-way ANOVA with Tukey's multiple comparisons test was used to test the difference in CA. There is no statistical difference in Fig. 3(d). **** indicates p < 0.0001.

"soft"; at the same time, the samples loaded with PNIPAM hydrogel could achieve larger displacement than the samples without grafting PNIPAM hydrogel. This indicated that both electrochemical treatment and loading PNIPAM hydrogel could reduce the surface hardness of the materials. The hardness and surface modulus of five points on the surface of the samples were randomly tested. According to the statistical chart of sample hardness [Fig. 2(b)], the hardness value of the NiTi sample is the largest (1.250 ± 0.330 GPa). The hardness values of the TiNL, PNIPAM/NiTi, and PNIPAM/TiNL samples gradually decreased to 1.051 ± 0.491 GPa, 0.909 ± 0.404 GPa, and 0.762 ± 0.384 GPa, respectively. Fig. 2(c) showed the numerical statistics of the surface modulus of the samples. The NiTi sample had a maximum surface modulus value: 95.952 ± 16.056 GPa. Due to the formation of the porous structure, the surface modulus value of the TiNL sample was significantly reduced to 28.866 ± 2.712 GPa. The PNIPAM hydrogel seemed to have little effect on the surface modulus of the samples. The surface modulus values of the PNIPAM/NiTi and PNIPAM/TiNL samples were 88.954 ± 11.466 GPa and 29.815 ± 6.989 GPa, respectively, which showed no obvious difference from those without PNIPAM hydrogel loading. The results in Fig. 2 proved that the nanoporous structure formed by electrochemical treatment had an impact on the surface mechanical properties of the samples. It could reduce the surface modulus and hardness, and the reduction in surface modulus was more significant. Moreover, the PNI-PAM hydrogel is smooth and has a flexible structure [35], which can further reduce the surface modulus and the hardness of the samples.

3.3. Thermosensitive and water locking abilities of the PNIPAM/TiNL sample

Surface wettability is another major factor that regulates the cell and bacterial adhesion behavior. The wettability of the different samples was shown in Fig. 3. When tested in the air, the WCA of the NiTi sample was 80.38 ± 5.03°(25 °C) or 80.83 ± 7.76 (37 °C), and the TiNL sample was more hydrophilic than the NiTi sample, whose WCA was 31.48 ± 7.24°(25°C) or 32.11 ± 14.28°(37°C) due to their porous structures. Both of the NiTi and TiNL samples possessed no temperature responsiveness, and their WCA remained constant no matter if tested at 25 °C or 37 °C. However, the WCA of the samples loaded with PNIPAM hydrogel showed a significant change when tested at different temperatures. For the PNIPAM/NiTi sample, the WCA increased from 37.58° ± 7.49° to 90.97° ± 3.74° when the temperature increased from 25 °C to 37 °C. The temperature responsiveness of the PNIPAM/TiNL sample was more obvious, and its WCA changed from 10.32 ± 15.67°(25 °C) to 116.14 ± 6.82°(37 °C) [Fig. 3(a) and (b)].

The thermal sensitivity of the PNIPAM-coated samples was derived from the temperature-controlled structure alteration of PNIPAM. Both hydrophilic and hydrophobic groups existed in PNIPAM; when the environmental temperature was lower than the LCST of PNIPAM (32 °C), the hydrophilic amide groups were exposed outside, which could bind with water molecules around through hydrogen bonds [36–38]. Hence, a hydration layer was formed on the PNIPAM hydrogel, resulting in the small WCA of the samples loaded with PNIPAM. However, when the temperature increased above the LCST, the hydrophobic interactions between the hydrophobic parts in PNIPAM increased, while the hydrogen bonds between PNIPAM and water molecules were weakened by random thermal motion [39,40]. The hydrophobic isopropyl groups in PNIPAM were then exposed outside, resulting in the high WCA of the PNIPAM-coated samples at 37 °C. The reason why PNIPAM/TiNL had a more significant temperature-sensitive regulation effect than PNI-PAM/NiTi could be explained by a traditional wetting model. The contact angle θ can be calculated by Young's equation as follows:

$$cos\,\theta = \left(\gamma_{sg} - \gamma_{sl}\right) / \gamma_{lg} \tag{1}$$

Where θ is the contact angle of a liquid droplet on a solid surface, γ_{sg} is the interfacial tension between solid and gas, γ_{sl} is the interfacial tension between solid and liquid, and γ_{lg} is the interfacial tension between liquid

and gas. Wenzel proposed a model describing the contact angle at a rough surface that is composed of solid and air as shown in Fig. 3(e)(ii) [41,42]. He modified Young's equation as follows:

$$cos\theta' = rcos\theta \qquad (2)$$

Where θ is the contact angle of a liquid droplet on a smooth surface in air, θ' is the contact angle of a liquid droplet on a rough surface in air, and r is the material surface roughness factor and is the ratio of the actual solid–liquid interface contact area S_A to the apparent contact area S_P, with $r \geq 1$. When the surface is hydrophobic, $90 < \theta < 180°$ and $cos\theta < 0$; then, it can be deduced that $cos\theta' < cos\theta$ and $\theta' > \theta$. This suggests that porous structures make hydrophobic surfaces more hydrophobic. When the surface is hydrophilic, $0 < \theta < 90°$ and $cos\theta > 0$; then, it can be deduced that $cos\theta' > cos\theta$ and $\theta' < \theta$. This suggests that porous structures make hydrophilic surfaces more hydrophilic. Therefore, the porous structure can regulate the wettability of the sample surface to some extent and can amplify the temperature-sensitive effect of the PNIPAM hydrogel, which makes the hydrophilicity and the hydrophobicity change of the PNIPAM/TiNL sample more obvious than that of the PNIPAM/NiTi sample.

Considering that the actual implantation environment of implants is rich in water and the cell membrane is nonpolar, an OCA test in the water system was conducted [43]. When the NiTi sample surface had porous TiO$_2$ structures, its OCA increased from $89.75 \pm 1.16°(25 °C)$ or $63.22 \pm 7.36°(37 °C)$ to an oleophobic state. The samples loaded with PNIPAM hydrogel showed excellent superoleophobic properties in the water system. The OCA of the PNIPAM/NiTi sample was $147.41° \pm 1.31°(25 °C)$ or $141.45° \pm 1.90°(37 °C)$, and the resistance of the PNIPAM/TiNL sample to oil droplets was better than that of the PNIPAM/NiTi sample. As shown in Fig. 3(e)(iii), the contact angle θ_3 can be calculated by Young's equation (1) as follows:

$$cos\theta_3 = \left(\gamma_{l_1-s}cos\theta_1 - \gamma_{l_2-s}cos\theta_2\right)/\left(\gamma_{l_1-l_2}\right) \qquad (3)$$

Where γ_{l_1-g} is the interfacial tension between liquid 1 and gas, θ_1 is the contact angle of liquid 1 in air, γ_{l_2-g} is the interfacial tension between liquid 2 and gas, θ_2 is the contact angle of liquid 2 in air, $\gamma_{l_1-l_2}$ is the interfacial tension between liquid 1 and liquid 2, and θ_3 is the contact angle of liquid 1 in liquid 2.

Water would be trapped below the oil droplet in the water system when the surface had porous structures. The apparent OCA (θ_3') in the water environment can be calculated by a Cassie–Baxter model as follows [Fig. 3(e)(iv)]:

$$cos\theta_3' = fcos\theta_3 + f - 1 \qquad (4)$$

Where f is the ratio of the contact area between the oil droplet and the solid surface to the total contact area between the oil droplet and the surface (the surface contains the solid surface and the interface of water in the pores), θ_3 is the contact angle of an oil droplet on a smooth surface in water, and θ_3' is the contact angle of an oil droplet on a rough surface in water [30,44]. The construction of a porous structure makes the pores rich in water molecules. One part of the oil droplet is in contact with the solid surface and the other part is in contact with the water molecules, which leads to $0 < f < 1$. Eq. (4) can be translated into $cos\theta_3' + 1 = f(cos\theta_3 + 1)$. As $0 < f < 1$, the equation can be further simplified as $cos\theta_3' < cos\theta_3$, with $\theta_3' > \theta_3$. Therefore, the OCA of the samples was increased because of the presence of the porous structure [45,46]. The TiNL sample thus tended to be more oleophobic due to the amount of water molecules trapped in the porous structures, reducing the contact area between the oil droplet and solid surface. When the contact area of the oil droplet and the solid surface was too small, the oil droplet had been unable to adhere to the sample surface. So the oil droplet left the

sample surface together with the dropper head. For the samples loaded with PNIPAM hydrogel, the PNIPAM hydrogel had a large hydrophilic molecular chain at 25 °C, which could capture water molecules on the hydrogel surface. It has been proved to be the main reason for oil resistance in water. At 37 °C, the surface of the PNIPAM/NiTi sample also unexpectedly showed oleophobicity, perhaps because the PNIPAM hydrophobic isopropyl group was exposed to the outer end and played a leading role in the oleophobicity. However, its surface oleophobicity was weaker than that of the PNIPAM/TiNL sample, which was due to the presence of the nanostructure on the surface of the PNIPAM/TiNL sample. In general, the loading of the PNIPAM hydrogel provided the surface of the samples with the ability where wettability varied with temperature, and the presence of the nanostructure could capture water molecules in the structure, thus improving the temperature sensitivity of the PNIPAM hydrogel and effectively preventing oil adhesion.

3.4. In vitro and in vivo antibacterial effects of the PNIPAM/TiNL sample

Gram-positive bacteria (*S. aureus*) and Gram-negative bacteria (*E. coli*) were selected as experimental strains to evaluate the antibacterial property of the different samples. Fig. 4(a) showed the fluorescence images of the live/dead stained bacteria cultured on various samples. At 25 °C, both *S. aureus* and *E. coli* survived in large numbers (stained to green) on the surface of the NiTi and TiNL samples, but almost no bacteria adhered to the surface of the PNIPAM/NiTi and PNIPAM/TiNL samples. At 37 °C, there were a large number of live bacteria on the surface of the NiTi and TiNL samples, and the fluorescence intensity on the surface of the samples was stronger than that at 25 °C. The number of bacteria on the surface of the PNIPAM/NiTi and PNIPAM/TiNL samples was significantly reduced compared with that of the NiTi and TiNL samples, and the fluorescence intensity of the PNIPAM/TiNL sample was the weakest. Fig. 4(b) showed the culture results of reinoculating the detached bacteria on the sample surface to the agar culture plates. At 25 °C, it could be seen from the agar culture plates that the bacteria separated from the NiTi and TiNL samples maintained a high activity, forming dense colonies. On the other hand, only a few bacterial colonies could be observed on the agar plates cultured with bacteria detached from the PNIPAM-coated samples. When the temperature was 37 °C, a large number of bacterial colonies grew on the agar plates with *S. aureus* or *E. coli* separated from the NiTi, TiNL, and PNIPAM/NiTi samples, whereas the number of bacterial colonies was significantly reduced for the PNIPAM/TiNL sample. Though the quantitative statistics of the anti-adhesion rate of the four samples to bacteria, it could be further confirmed that the inhibition rate of the PNIPAM/TiNL sample was higher than 90% at both 25 °C and 37 °C. And the PNIPAM/NiTi sample had the same ability to inhibit bacterial adhesion as the PNIPAM/TiNL sample at 25 °C, however, its anti-adhesion ability showed a significant decline at 37 °C (Table S2). The integrity and morphology of the bacterial cell membrane were observed by SEM. Fig. 4(c) showed the SEM morphology of *S. aureus* and *E. coli* on the surface of the four samples at 25 °C and 37 °C. It showed that *S. aureus* on the surface of the four samples was all smooth and flat in shape, with almost no dead bacteria, but the number of *S. aureus* varied greatly: a large quantity of *S. aureus* existed on the surface of the NiTi and TiNL samples, and most of the bacteria were agglomerated together, which was more common at 37 °C. However, the number of *S. aureus* on the surface of the PNIPAM/NiTi and PNIPAM/TiNL samples significantly decreased at 25 °C, with only a few individual bacteria present. At 37 °C, there were still a lot of aggregated bacteria on the surface of the PNIPAM/NiTi sample, and the number was slightly lower than that of the NiTi and TiNL samples; however, only a few individual bacteria existed on the surface of the PNIPAM/TiNL sample. Accordingly, *E. coli* adhering to the surface of the four samples was rod-shaped with complete structure and good survival, and the quantity difference was similar to that of *S. aureus*. The result was in good agreement with that of agar plate and live/dead staining, suggesting that
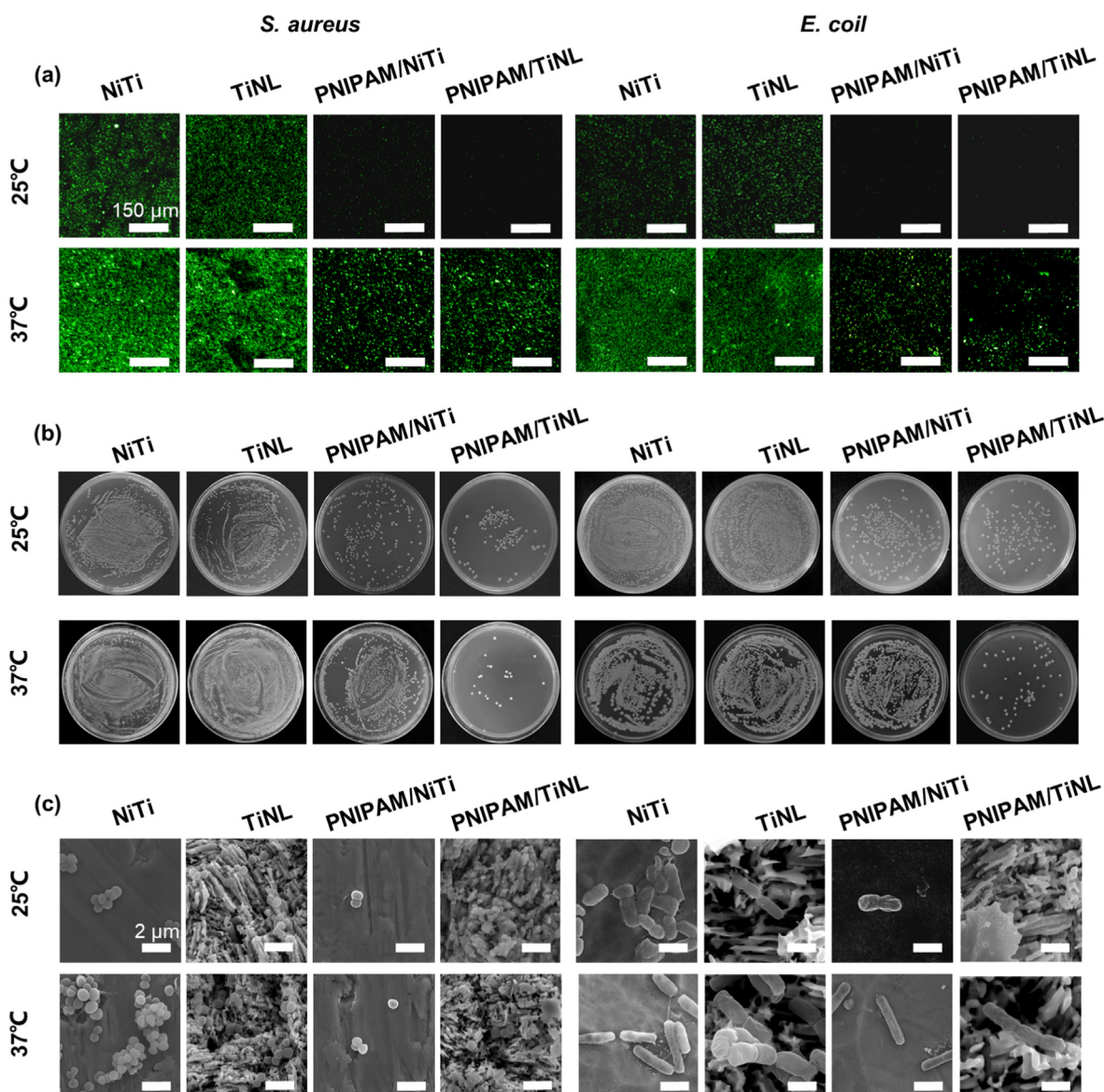
Fig. 4. (a) Fluorescence images of live/dead staining of cultured *S. aureus* and *E. coli* on the surface of the four samples at 25 °C and 37 °C; (b) *S. aureus* and *E. coli* bacterial distribution on the surface of the four samples at 25 °C and 37 °C; (c) SEM images of *S. aureus* and *E. coli* on the four samples at 25 °C and 37 °C.

the PNIPAM/NiTi sample only presented good bacterial inhibition ability at 25 °C, whereas the PNIPAM/TiNL sample exhibited preferable bacteriostasis effect at both 25 °C and 37 °C.

To evaluate the bacterial inhibition efficiency of the samples *in vivo*, the *E. coli*-contaminated samples were implanted subcutaneously in mice. All the wounds on the back of the mice began to heal gradually 3 days after implantation without obvious suppuration and infection [Figure S4(a)]. The samples were taken from the mice and slid on the agar plate for a long distance. After 16 h, the number of bacterial colonies was observed [Figure S4(b)]. At the same time, the bacterial morphology on the sample surface was observed by SEM [Fig. 5(a)]. *E. coli* appeared in good shape and aggregated on the NiTi, TiNL, and PNIPAM/NiTi samples. The number of bacteria on the surface of the PNIPAM/TiNL sample was few, which was in accordance with the experiments *in vitro*, demonstrating the effective bacterial inhibition capacity of the PNIPAM/TiNL sample. At the same time, the skin in contact with the samples was stained, and the histological sections were observed [Fig. 5(b) and (c)]. The infections usually facilitate the immunologic system to recruit abundant inflammatory cells [47]. From the tissue section, the thickness of the fibrous layer formed (black arrows) and the number of neutrophils

(red arrows) in the surrounding tissue of the sample could be clearly seen, which can quantitatively evaluate the degree of inflammation. It could be seen that there was no significant difference in the number of neutrophils among the four groups. On the other hand, the tissue around the PNIPAM/TiNL sample presented the thinnest fiber layer, showing that the degree of bacterial infection of the PNIPAM/TiNL group was the lowest. To investigate the toxic effects of the PNIPAM/TiNL sample on other organs of the mice, histological studies had been carried out on the major organs of the bacteria-infected mice, and the images were presented in Fig. 5(f). No lesions or abnormalities were found in all major organs (heart, liver, spleen, lung, and kidney) of the four samples, which indicated that all of the four samples were very safe. The data of the blood routine and biochemical tests (Figure S5) in the mice also confirmed this point. In conclusion, the NiTi and TiNL samples did not inhibit bacterial adhesion, and many bacteria that remained *in vivo* were clustered together, which might induce the formation of biofilm and increase the risk of implant failure due to bacterial infection. The PNIPAM/NiTi sample maintained good antibacterial performance at 25 °C, but this ability was weakened at 37 °C; hence, the PNIPAM/NiTi sample could not prevent bacterial adhesion when implanted into the body. The
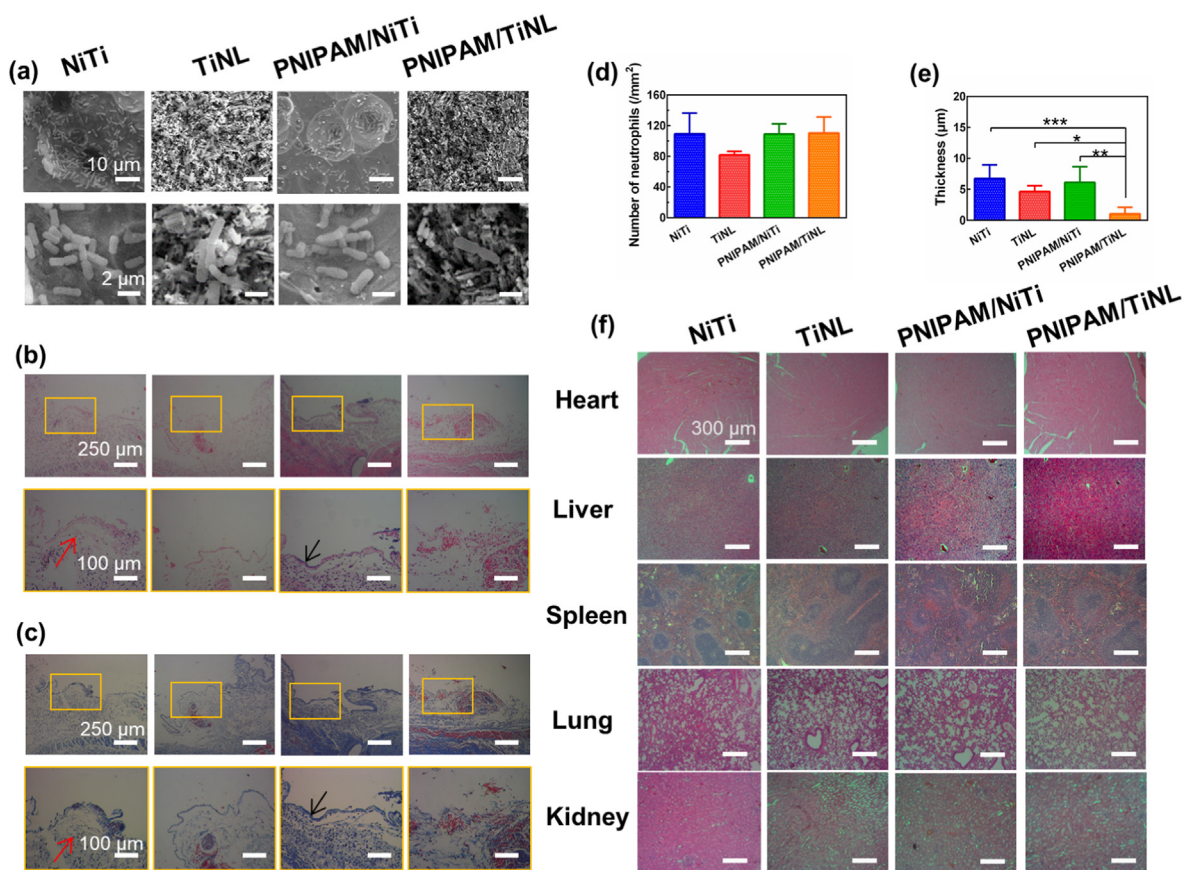
Fig. 5. (a) SEM images of *E. coli in vivo* at 3 days; optical images of (b) HE- and (c) MASSON-stained tissues in direct contact with the four samples at 3 days; (d) number of neutrophils and (e) thickness of the fibrous layer for the tissue in contact with the four samples; (f) histological changes in various tissues of the mice implanted with the four samples. One-way ANOVA with Tukey's multiple comparisons test was used to test the difference in number of neutrophils and thickness of the fibrous layer. There is no statistical difference in Fig. 5(d). * indicates $p < 0.05$, ** indicates $p < 0.01$, *** indicates $p < 0.001$.

PNIPAM/TiNL sample maintained good bacteriostatic ability at both 25 °C and 37 °C. Therefore, the PNIPAM/TiNL sample not only prevented preoperative and intraoperative infection but also reduced postoperative bacterial infection in the mice without inducing any negative effects.

Combined with the contact angle of the samples and previous literature studies, a reasonable explanation of the antibacterial mechanism of the samples is proposed. To the best of our knowledge, it is difficult for bacteria to adhere to a surface rich in hydration layer [48,49]. As PNIPAM hydrogel is temperature sensitive, when it is at 25 °C, the surface of PNIPAM is rich in hydration layer, and it has a particularly low interfacial energy with water; moreover, the absorption of protein on it is not thermodynamically favorable because it will result in entropy loss, which provides the antibacterial mechanism of the PNIPAM/NiTi and PNIPAM/TiNL samples at 25 °C [50]. However, the PNIPAM chains are in a hydrophobic state, the surface water content is reduced, and the hydration layer collapses, allowing bacteria to adsorb at 37 °C. The exposure of the PNIPAM hydrophobic isopropyl group still has a negative effect on bacterial adhesion. On the contrary, a smooth surface provides enough adhesion sites for bacteria, so the antibacterial ability of the PNIPAM/NiTi sample is greatly weakened at 37 °C but does not completely disappear. For the PNIPAM/TiNL surface, due to the presence of the porous structure, water molecules are trapped in the porous structures, resulting in a higher hydration rate on the surface. The only adhesion sites for bacteria are the bulge of the porous structures loaded with hydrophobic isopropyl, which reduces the bacterial adhesion rate on the sample surface. The OCA results in water verify this effect. Hence, the temperature sensitivity of PNIPAM hydrogel and the water-locking effect of the nanoporous structures together ensure that the PNIPAM/TiNL sample has a high hydration rate and a small number of surface contact

sites, which make the surface of the PNIPAM/TiNL sample to have good antibacterial performance even at temperatures above the LCST.

3.5. In vitro and in vivo cytocompatibility of the PNIPAM/TiNL sample

Preferable osteogenesis performance is also important for orthopedic implants and systemically evaluated in the study. The initial adhesion behavior of the rBMSCs on the surface of the NiTi, TiNL, PNIPAM/NiTi, and PNIPAM/TiNL samples was shown in Fig. 6(a). A lot of cells were found to adhere to the surface of the four samples, and there was no difference in the number of cells. In addition, with the increase in culture time, the cells spread evenly on each surface, which proved that the presence of the thermosensitive hydrogel and nanostructure had no obvious effect on cell adhesion. In particular, the initial cell adhesion to the surface of the PNIPAM/TiNL sample with good antibacterial property was not hindered, because the contact area between the larger cells and sample surface was much larger than that between the bacteria and sample surface; accordingly, more contact sites of a cell made cell adhesion easier. Fig. 6(b) and (c) showed the proliferation of the rBMSCs growing on the surface of the four samples. It could be seen that the number of cells on the surface of the different samples increased with time during the experiment, and there was almost no difference in cell viability after 1 and 4 days of culture, which was further confirmed by the live/dead staining results [Fig. 6(c)]. After 7 days of culture, the number of rBMSCs on the surface of the TiNL sample was the largest, while the number of rBMSCs on the surface of the PNIPAM/TiNL sample was slightly lower than that of the other three groups. The results of *S. aureus* and rBMSCs co-culture demonstrated large amounts of cell adhesion on the surface of the PNIPAM/TiNL sample, whereas the PNIPAM/NiTi
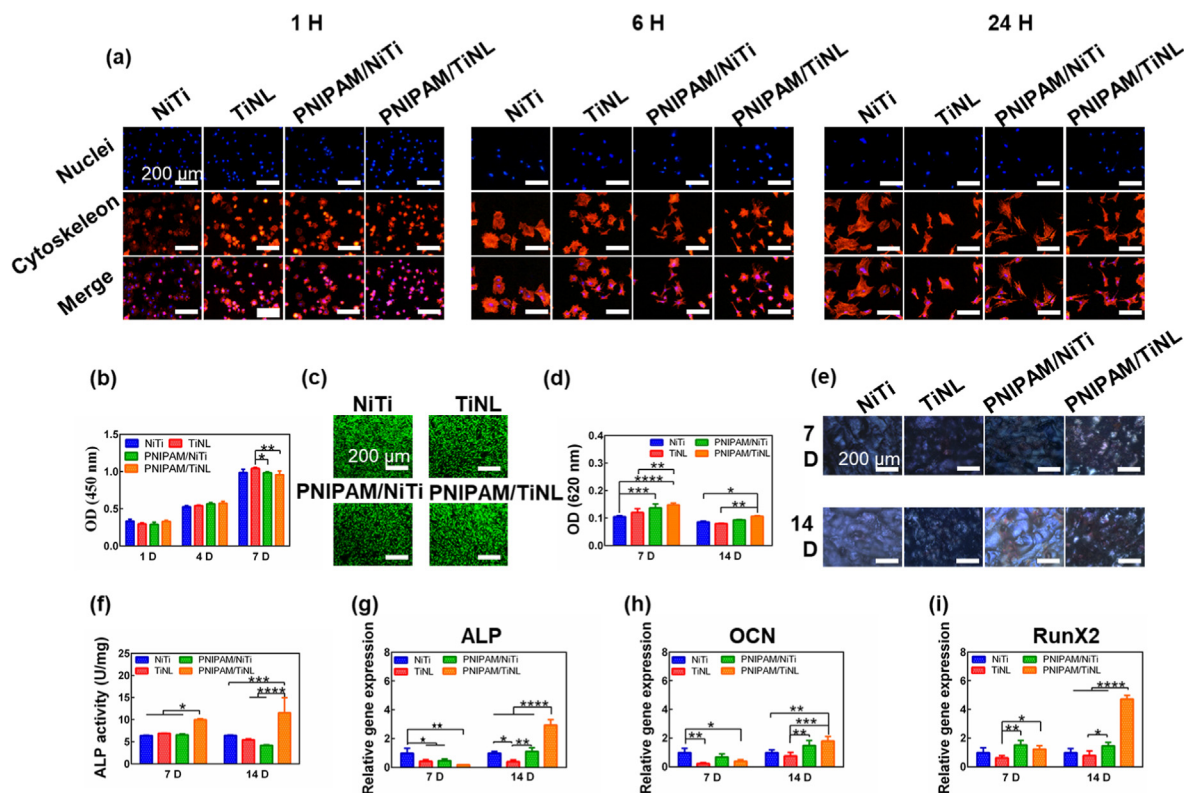
Fig. 6. (a) Fluorescent staining of rBMSCs after culturing for 1, 6, and 24 h (the nucleus was visualized with blue fluorescence, whereas the cytoskeleton was visualized with red fluorescence); (b) CCK-8 assay of cell viabilities cultured in the medium with the different samples after 1, 4, and 7 days of culture; (c) live/dead staining fluorescence microscopic images of the four samples at 4 days of culture; (d) quantitative measurement of ECM secreted by the rBMSCs after 7 and 14 days of culture; (e) optical microscopy of collagen at 7 and 14 days of culture; (f) ALP activities of rBMSCs cultured in the medium with the different samples after 7 and 14 days of culture; the expression of (g) the ALP, (h) OCN, and (i) RunX2 genes in the rBMSCs was analyzed by RT-PCR after culturing for 7 and 14 days. Two-way ANOVA with Tukey's multiple comparisons test was used to test the difference in rBMSCs proliferation and osteogenic differentiation. * indicates $p < 0.05$, ** indicates $p < 0.01$, *** indicates $p < 0.001$, **** indicates $p < 0.0001$.

sample occupied the surface by bacteria due to its weak ability to inhibit bacterial adhesion (Figure S3 and Note S2). The adhesion of bacteria and cells to sample surface is competitive. Therefore, the number of the rBMSCs on the PNIPAM/NiTi sample surface was very small and the survival rate of the rBMSCs was relatively low. The above results showed that the water-locked effect of porous structures did play a unique role in antibacterial effect, ensuring that the PNIPAM/TiNL sample can inhibit bacterial adhesion and have no negative effect on cell adhesion.

ECM secreted by cells not only supports and nourishes tissue cells but also is closely related to cell proliferation and differentiation [51]. Fig. 6(d) quantitatively demonstrated the ECM secreted by the rBMSCs cultured on the different samples, which showed the trend of PNI-PAM/TiNL > PNIPAM/NiTi > NiTi and TiNL. This could be confirmed from Fig. 6(e) that showed the optical images. Only small areas of calcium nodules (stained red by ARS) were appeared on the surface of the NiTi sample at both 7 and 14 days, while the area of calcium nodules formed by rBMSCs mineralization on the surface of the PNIPAM/TiNL sample increased significantly under the same conditions. ALP is a characteristic protein that plays as an early marker of bone formation during osteoblast differentiation [52–54]. As shown in Fig. 6(f), after 7 days of culture, the active expression of ALP of the rBMSCs on the surface of the PNIPAM/TiNL sample was significantly higher than that of the other samples, and the difference was further increased after 14 days of culture. Fig. 6(g)–(i) showed the quantitative expression results of the ALP, OCN, and RunX2 genes in the rBMSCs, respectively, after 7 and 14 days of culture by PCR testing. The expression of these three genes was indicative of the degree of osteogenic differentiation. After 7 days of culture, the gene expression of ALP and OCN of the rBMSCs on the surface of the NiTi sample was slightly higher than that of other samples,

and the expression of RunX2 was no different from that of the PNI-PAM/TiNL sample. This indicated that the PNIPAM/TiNL sample did not have obvious effect on osteogenic differentiation within 7 days. However, when the incubation time was increased to 14 days, the expression of the three genes in the cells cultured on the PNIPAM/TiNL sample was significantly increased and much higher than those of the other three groups. It has been reported that cell proliferation and differentiation are two competitive processes, and high differentiation activity usually causes low proliferation rate [55]. Therefore, the rBMSCs cultured on the surface of the TiNL sample for 7 days had a high proliferation rate, and correspondingly, its differentiation effect was weak. The PNIPAM/TiNL sample presented the opposite effect. Judging from the results of ECM, ALP, and gene expression, the PNIPAM/TiNL sample had a positive effect on cell differentiation and was more dominant in long-term differentiation than in short-term differentiation.

Blood vessels are thought to influence the osteogenic generation of new bones [56,57]. The angiogenesis ability of the various samples was evaluated by culturing HUVECs. Fig. 7(a) showed the adhesion behavior of the HUVECs after 12 h of coculture with the different samples. After 1 and 6 h of culture, the cells were spherical in shape, and there was no difference in the number of cells. With the increase in culture time, the cells spread out and changed from the initial spherical shape to an irregular polygonal shape. The live/dead staining [Fig. 7(b)] results showed that nearly no dead cells were observed on the surface of the four samples, and there was no significant difference in the fluorescence intensity of living cells. Fig. 7(c) showed a similar situation to the live/dead staining results. The number of cells on the surface of the TiNL sample was the highest after 12 h of culture, whereas that of the NiTi sample was the least; however, in general, the difference between the four samples
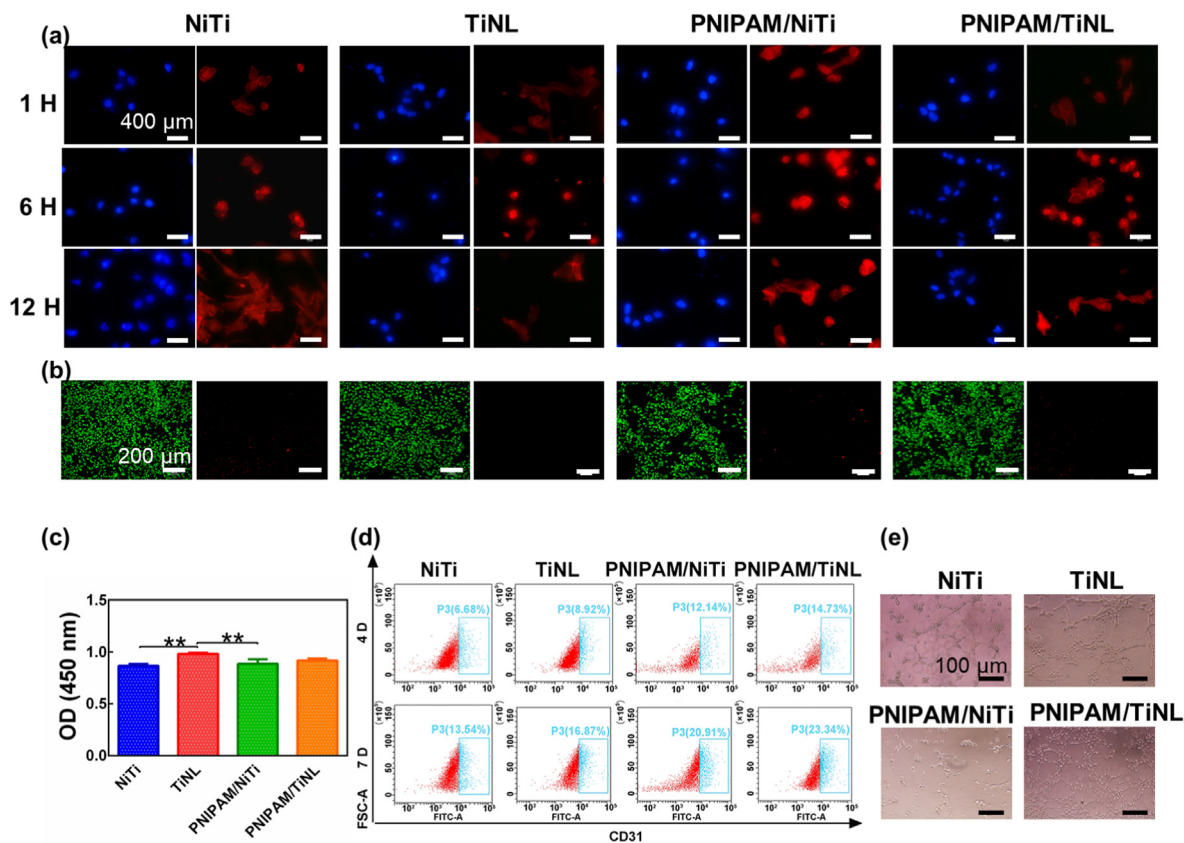
Fig. 7. (a) Fluorescent staining of HUVECs after culturing for 1, 6, and 12 h (the nucleus was visualized with blue fluorescence, whereas the cytoskeleton was visualized with red fluorescence); (b) live/dead staining fluorescence microscopic images of the four samples at 1 day of culture; (c) CCK-8 assay of cell viabilities cultured in the medium with the different samples after 1 day of culture; (d) flow cytometry graph plots of CD31; (e) *in vitro* angiogenesis of the HUVECs cultured with the four samples. One-way ANOVA with Tukey's multiple comparisons test was used to test the difference in HUVECs proliferation. ** indicates $p < 0.01$.

was not significant. Platelet endothelial cell adhesion molecule 1 (CD31) plays an important role in regulating endothelial cell adhesion and angiogenesis [58]. The flow cytometry results showed the quantification expression of CD31 [Fig. 7(d)]. The expression level of CD31 in the HUVECs of the NiTi sample was 6.68% (4 days) or 13.54% (7 days). The expression level of CD31 in the HUVECs of the modified groups was all higher than that of the NiTi sample no matter at 4 days or 7 days, among which the PNIPAM/TiNL group presented the highest expression level, which was 14.73% (4 days) or 23.34% (7 days). Tube formation assay was used to evaluate the angiogenesis activity, and the result was shown in Fig. 7(e). It could be observed distinctly that there were more tube network structures in the PNIPAM/TiNL group than in the other groups. The above results suggested that, although the PNIPAM/TiNL sample showed no ability in promoting cell adhesion and proliferation, it was most conductive to the formation of blood vessels compared with the other samples. This may be due to the fact that the Ni^{2+} release of the PNIPAM/TiNL sample is in the appropriate range for promoting angiogenesis (Figure S6) [54].

Encouraged by the preferable results of the *in vitro* experiments, *in vivo* experiments on animals were conducted to confirm the osteogenic ability of the PNIPAM/TiNL sample [Fig. 8(a)]. Fig. 8(b) showed the reconstructed Micro-CT images of the bone formation around the different implants after 8 weeks of implantation. The implants were marked with white colour, and new bones were marked with yellow colour. The fewest new bones appeared around the NiTi sample among the four types of implants, whereas the most new bone formed around the PNIPAM/TiNL sample. The above findings were further verified by the quantitative results of bone volume/total volume [Fig. 8(c)], trabecular thickness [Fig. 8(d)], and bone mineral density [Fig. 8(e)]. Histological staining of the axial sections of the specimens showed the details of the

bone–implant interface and the peri-implant bone tissue after 8 weeks of implantation [Fig. 8(f)]. The area of the new bone (stained red) formed around the PNIPAM/TiNL implant was slightly larger than those of the other three groups. In addition, an obvious gap between the newly formed bone and implant surface could be observed in the NiTi group, whereas the other implants, especially the PNIPAM/TiNL implant, were tightly integrated with the newly formed bone. Likewise, the Micro-CT images of the bone formation after 12 weeks of implantation showed a similar trend [Fig. 8(g)]. The new bone around the four implants increased compared with that of 8 weeks. The PNIPAM/TiNL sample still showed the best osteogenesis promotion ability compared with the other samples, which was verified by the quantitative results of bone volume/total volume [Fig. 8(h)], trabecular thickness [Fig. 8(i)], and BMD [Fig. 8(j)]. Fig. 8(k) showed that there is significantly more new bone forming around the PNIPAM/TiNL implant. In addition, the integration of the newly formed bone and PNIPAM/TiNL sample was the tightest among all the samples, demonstrating its great *in vivo* osseointegration. The excellent osteogenic ability exhibited by the PNIPAM/TiNL sample is related to the PNIPAM loading and low surface modulus and hardness. PNIPAM has good biocompatibility, and the exposed hydrophobic isopropyl segment attracts the protein containing hydrophobic chains, which allows cells to adhere to the surface. Moreover, compared with other samples, the surface modulus and hardness of PNIPAM/TiNL sample are the lowest. The stiff matrix induces strong cell traction (contraction) forces which increases cell adhesion strength and correlates inversely with cell migration speed. Therefore, cells prefer to adhere to the surface of the PNIPAM/TiNL sample; at the same time, the PNIPAM/TiNL sample can distribute the compressive force evenly during loading, ensuring the integration of the bone and the implants.

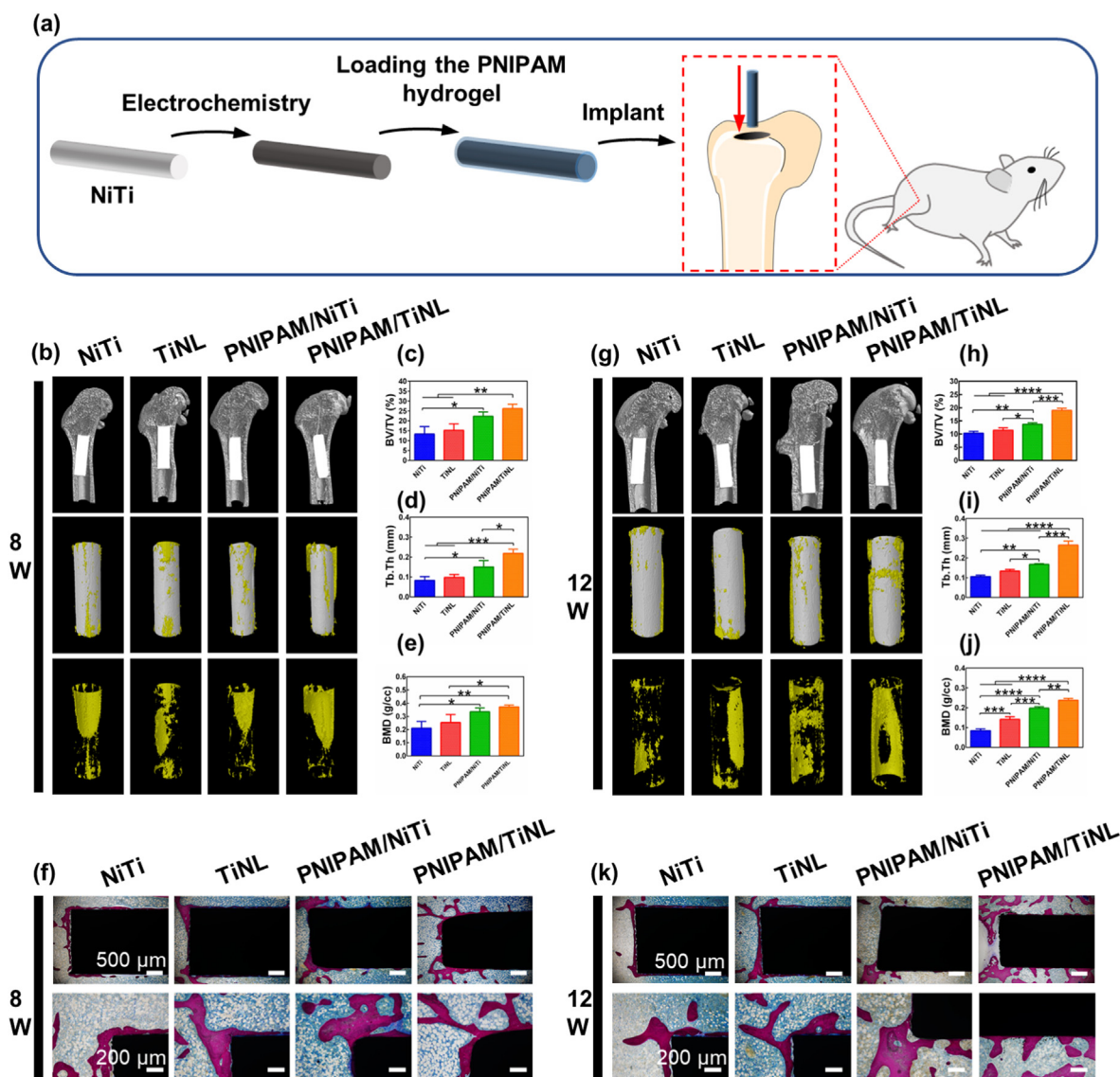In general, at 25 °C, the hydrophilic amide group of PNIPAM has a

Fig. 8. (a) Experimental flow chart of the samples implanted in the femur; 3D Micro-CT images of the implants and the peri-implant bone tissue (b) 8 and (g) 12 weeks after implantation; quantitative statistics of bone volume/total volume (BV/TV) at (c) 8 and (h) 12 weeks, trabecular thickness (Tb·Th) at (d) 8 and (i) 12 weeks, and bone mineral density (BMD) at (e) 8 and (j) 12 weeks; optical images of the peri-implant bone tissue by HE staining (f) 8 and (k) 12 weeks after implantation. One-way ANOVA with Tukey's multiple comparisons test was used to test the difference in BV/TV, Tb·Th and BMD. * indicates $p < 0.05$, ** indicates $p < 0.01$, *** indicates $p < 0.001$, **** indicates $p < 0.0001$.

strong hydrogen bond with water molecules. After PNIPAM absorbs water, the water molecules are regularly arranged on the surface. The surface of the PNIPAM/TiNL sample is rich in hydration layer, and bacteria cannot adhere to the surface. Therefore, the PNIPAM/TiNL sample has good bacteriostatic properties. The hydration layer of PNIPAM collapses for the PNIPAM/TiNL sample, and the nanoporous structures can trap water molecules firmly at 37 °C. Therefore, the contact sites of bacteria on the surface of the PNIPAM/TiNL sample can only be the bulges of porous structures, and the number of contact sites is decreased, so that the PNIPAM/TiNL sample has good performance of inhibiting bacterial adhesion. Cells are much larger than bacteria and have far more sites of attachment than bacteria, so their adhesion is not inhibited. Moreover, low surface modulus and hardness are more favorable for cell growth and osseointegration, and the Ni^{2+} release of the PNIPAM/TiNL sample can promote angiogenesis to a certain extent, which can deliver nutrients for the formation of new bone. Therefore, the PNIPAM/TiNL sample shows the best bacteriostatic properties and osseointegration effects.

4. Conclusions

In summary, porous structures loaded with thermosensitive PNIPAM hydrogel constructed on a NiTi surface were reported. At 25 °C, due to the existence of the hydration layer of the thermosensitive PNIPAM hydrogel, the bacteria could be repelled on the sample surface. Under the influence of temperature change, the hydration layer on the surface of the PNIPAM hydrogel disappeared at 37 °C. However, the porous structures retained water molecules within the pores, and this water-locking effect maintained a high hydration rate on the surface, making bacterial adhesion difficult due to the reduction of adhesion sites. The volume of cells is much larger than that of bacteria, so the contact area of the cells on the sample surface is also larger than that of the bacteria. Therefore, cell adhesion is not affected by the water-locking effect. In addition, *in vivo* experiments demonstrated that the sample had excellent ability to inhibit bacterial adhesion and bone integration. We believe that our work will expand the application of PNIPAM in biomaterials and provide additional ideas for the surface modification of implants.

Credit author statement

Xueqing Hao: Methodology, Data curation, Visualization, Writing – original draft. **Jielong Zhou**: Investigation, Methodology, Writing – review & editing. **Juning Xie**: Writing – review & editing. **Xianrui Zou**: Data curation. **Baoe Li**: Data curation. **Chunyong Liang**: Conceptualization, Project administration, Visualization. **Yu Zhang**: Visualization. **Feng Peng**: Funding acquisition, Validation. **Donghui Wang**: Validation, Supervision, Funding acquisition.

Data availability

The processed data required to reproduce these findings cannot be shared at this time as the data also forms part of an ongoing study.

Declaration of competing interest

The authors declare that they have no known competing financial interests or personal relationships that could have appeared to influence the work reported in this paper.

Appendix A. Supplementary data

Supplementary data to this article can be found online at https://doi.org/10.1016/j.mtbio.2022.100285.

References

[1] J. Lin, J. Hu, W. Wang, K. Liu, C. Zhou, Z. Liu, S. Kong, S. Lin, Y. Deng, Z. Guo, Thermo and light-responsive strategies of smart titanium-containing composite material surface for enhancing bacterially anti-adhesive property, J. Chem. Eng. Jpn. 407 (2021), https://doi.org/10.1016/j.cej.2020.125783.

[2] E. Zhang, X. Zhao, J. Hu, R. Wang, S. Fu, G. Qin, Antibacterial metals and alloys for potential biomedical implants, J. Bioact Mater 6 (2021) 2569–2612, https://doi.org/10.1016/j.bioactmat.2021.01.030.

[3] Z. Weng, L. Bai, Y. Liu, Y. Zhao, Y. Sun, X. Zhang, X. Huang, D. Huang, X. Yao, R. Hang, Osteogenic activity, antibacterial ability, and Ni release of Mg-incorporated Ni-Ti-O nanopore coatings on NiTi alloy, J. Appl Surf Sci 486 (2019) 441–451, https://doi.org/10.1016/j.apsusc.2019.04.259.

[4] E.T. Rochford, R.G. Richards, T.F. Moriarty, Influence of material on the development of device-associated infections, J. Clin Microbiol Infect 18 (2012) 1162–1167, https://doi.org/10.1111/j.1469-0691.2012.04002.x.

[5] Y.L. Zhang, J. Liu, M.W. Chen, P.F. Gao, Y. Gong, R. Chen, Y. Tang, W.H. Yang, K.Y. Cai, Photolithographic-based stamp technique for improving the biocompatibility of antibacterial titanium implant by dynamic clearance of antibacterial agents, J. Chem. Eng. Jpn. 421 (2021), https://doi.org/10.1016/j.cej.2021.129756.

[6] B. Wang, Z. Wu, J. Lan, Y. Li, L. Xie, X. Huang, A. Zhang, H. Qiao, X. Chang, H. Lin, H. Zhang, T. Li, Y. Huang, Surface modification of titanium implants by silk fibroin/Ag co-functionalized strontium titanate nanotubes for inhibition of bacterial-associated infection and enhancement of in vivo osseointegration, J. Surf Coat Tech 405 (2021) 126700, https://doi.org/10.1016/j.surfcoat.2020.126700.

[7] L. Zhang, C. Ning, T. Zhou, X. Liu, K.W. Yeung, T. Zhang, Z. Xu, X. Wang, S. Wu, P.K. Chu, Polymeric nanoarchitectures on Ti-based implants for antibacterial applications, J. ACS Appl Mater Interfaces 6 (2014) 17323–17345, https://doi.org/10.1021/am5045604.

[8] S.B. Goodman, Z. Yao, M. Keeney, F. Yang, The future of biologic coatings for orthopaedic implants, J. Biomaterials 34 (2013) 3174–3183, https://doi.org/10.1016/j.biomaterials.2013.01.074.

[9] C. Mas-Moruno, B. Su, M.J. Dalby, Multifunctional coatings and nanotopographies: toward cell instructive and antibacterial implants, J. Adv Healthc Mater 8 (2019), e1801103, https://doi.org/10.1002/adhm.201801103.

[10] B. Wang, Y. Li, S. Wang, F. Jia, A. Bian, K. Wang, L. Xie, K. Yan, H. Qiao, H. Lin, J. Lan, Y. Huang, Electrodeposited dopamine/strontium-doped hydroxyapatite composite coating on pure zinc for anti-corrosion, antimicrobial and osteogenesis, J. Mater Sci Eng C Mater Biol Appl 129 (2021) 112387, https://doi.org/10.1016/j.msec.2021.112387.

[11] W. He, Y. Zhang, J. Li, Y. Gao, F. Luo, H. Tan, K. Wang, Q. Fu, A novel surface structure consisting of contact-active antibacterial upper-layer and antifouling sub-layer derived from gemini quaternary ammonium salt polyurethanes, J. Sci Rep 6 (2016) 32140, https://doi.org/10.1038/srep32140.

[12] H.J. Busscher, H.C. van der Mei, G. Subbiahdoss, P.C. Jutte, J.J. van den Dungen, S.A. Zaat, M.J. Schultz, D.W. Grainger, Biomaterial-associated infection: locating the finish line in the race for the surface, J. Sci Transl Med 4 (2012) 153rv110, https://doi.org/10.1126/scitranslmed.3004528.

[13] T. Qiu, Q. Zeng, N. Ao, Preparation and characterization of chlorinated nature rubber (CNR) based polymeric quaternary salt bactericide, J. Mater Lett 122 (2014) 13–16, https://doi.org/10.1016/j.matlet.2014.01.135.

[14] M.D. Seo, H.S. Won, J.H. Kim, T. Mishig-Ochir, B.J. Lee, Antimicrobial peptides for therapeutic applications: a review, J. Molecules 17 (2012) 12276–12286, https://doi.org/10.3390/molecules171012276.

[15] C. Su, Y. Hu, Q. Song, Y. Ye, L. Gao, P. Li, T. Ye, Initiated chemical vapor deposition of graded polymer coatings enabling antibacterial, antifouling, and biocompatible surfaces, J. ACS Appl Mater Interfaces 12 (2020) 18978–18986, https://doi.org/10.1021/acsami.9b22611.

[16] B. Wang, Q. Xu, Z. Ye, H. Liu, Q. Lin, K. Nan, Y. Li, Y. Wang, L. Qi, H. Chen, Copolymer brushes with temperature-triggered, reversibly switchable bactericidal and antifouling properties for biomaterial surfaces, J. ACS Appl Mater Interfaces 8 (2016) 27207–27217, https://doi.org/10.1021/acsami.6b08893.

[17] T. Wei, Q. Yu, H. Chen, Responsive and Synergistic Antibacterial coatings: fighting against bacteria in a smart and effective way, J. Adv Healthc Mater 8 (2019) 1801381, https://doi.org/10.1002/adhm.201801381.

[18] Q. Yu, Z.Q. Wu, H. Chen, Dual-function antibacterial surfaces for biomedical applications, J. Acta Biomater 16 (2015) 1–13, https://doi.org/10.1016/j.actbio.2015.01.018.

[19] M. Hoyos-Nogues, J. Buxadera-Palomero, M.P. Ginebra, J.M. Manero, F.J. Gil, C. Mas-Moruno, All-in-one trifunctional strategy: a cell adhesive, bacteriostatic and bactericidal coating for titanium implants, J. Colloids Surf B Biointerfaces 169 (2018) 30–40, https://doi.org/10.1016/j.colsurfb.2018.04.050.

[20] Y. Miao, X. Shi, Q. Li, L. Hao, L. Liu, X. Liu, Y. Chen, Y. Wang, Engineering natural matrices with black phosphorus nanosheets to generate multi-functional therapeutic nanocomposite hydrogels, J. Biomater Sci 7 (2019) 4046–4059, https://doi.org/10.1039/c9bm01072f.

[21] X. Wang, S. Yan, L. Song, H. Shi, H. Yang, S. Luan, Y. Huang, J. Yin, A.F. Khan, J. Zhao, Temperature-responsive hierarchical polymer brushes switching from bactericidal to cell repellency, J. ACS Appl Mater Interfaces 9 (2017) 40930–40939, https://doi.org/10.1021/acsami.7b09968.

[22] K. Page, M. Wilson, I.P. Parkin, Antimicrobial surfaces and their potential in reducing the role of the inanimate environment in the incidence of hospital-acquired infections, J. J Mater Chem 19 (2009), https://doi.org/10.1039/b818698g.

[23] B. Li, J. Ma, D. Wang, X. Liu, H. Li, L. Zhou, C. Liang, H. Wang, Self-adjusting antibacterial properties of Ag-incorporated nanotubes on micro-nanostructured Ti surfaces, J. Biomater Sci 7 (2019) 4075–4087, https://doi.org/10.1039/c9bm00862d.

[24] X. Sun, P. Tyagi, S. Agate, M.G. McCord, L.A. Lucia, L. Pal, Highly tunable bioadhesion and optics of 3D printable PNIPAm/cellulose nanofibrils hydrogels, J. Carbohydr Polym 234 (2020) 115898, https://doi.org/10.1016/j.carbpol.2020.115898.

[25] D. Roy, W.L. Brooks, B.S. Sumerlin, New directions in thermoresponsive polymers, J. Chem Soc Rev 42 (2013) 7214–7243, https://doi.org/10.1039/c3cs35499g.

[26] R.B. Vasani, S.J. McInnes, M.A. Cole, A.M. Jani, A.V. Ellis, N.H. Voelcker, Stimulus-responsiveness and drug release from porous silicon films ATRP-grafted with poly(N-isopropylacrylamide), J. Langmuir 27 (2011) 7843–7853, https://doi.org/10.1021/la200551g.

[27] R. Hang, F. Zhao, X. Yao, B. Tang, P.K. Chu, Self-assembled anodization of NiTi alloys for biomedical applications, J. Appl Surf Sci 517 (2020), https://doi.org/10.1016/j.apsusc.2020.146118.

[28] P. Roy, S. Berger, P. Schmuki, TiO2 nanotubes: synthesis and applications, J. Angew Chem Int Ed Engl 50 (2011) 2904–2939, https://doi.org/10.1002/anie.201001374.

[29] F.J. Xu, S.P. Zhong, Y.L. Yung, E.T. Kang, K.G. Neoh, Surface-active and stimuli-responsive polymer-Si(100) hybrids from surface-initiates atom transfer radical polymerization for control of cell adhesion, J. Biomacromolecules 5 (2004) 2392–2403, https://doi.org/10.1021/bm049675a.

[30] L. Chen, M. Liu, H. Bai, P. Chen, F. Xia, D. Han, L. Jiang, Antiplatelet and thermally responsive poly(N-isopropylacrylamide) surface with nanoscale topography, J. J Am Chem Soc 131 (2009) 10467–10472, https://doi.org/10.1021/ja9019935.

[31] G. Zou, J. Shen, P. Duan, X. Xia, R. Chen, B. Jin, Temperature-sensitive poly(N-isopropylacrylamide)/konjac glucomannan/graphene oxide composite membranes with improved mechanical property, swelling capability, and degradability, J. Int J Polym Sci 2018 (2018) 1–10, https://doi.org/10.1155/2018/7906747.

[32] S. Belali, H. Savoie, J.M. O'Brien, A.A. Cafolla, B. O'Connell, A.R. Karimi, R.W. Boyle, M.O. Senge, Synthesis and characterization of temperature-sensitive and chemically cross-linked poly(N-isopropylacrylamide)/photosensitizer hydrogels for applications in photodynamic therapy, J. Biomacromolecules 19 (2018) 1592–1601, https://doi.org/10.1021/acs.biomac.8b00293.

[33] Y. Liu, P.P. Chen, W.Y. Nie, Y.F. Zhou, Fabrication of a temperature-responsive and recyclable MoS2 nanocatalyst through composting with poly (N-isopropylacrylamide), J. Appl Surf Sci 436 (2018) 562–569, https://doi.org/10.1016/j.apsusc.2017.12.080.

[34] M. Kaur, K. Singh, Review on titanium and titanium based alloys as biomaterials for orthopaedic applications, J. Mater Sci Eng C Mater Biol Appl 102 (2019) 844–862, https://doi.org/10.1016/j.msec.2019.04.064.

[35] E. Liu, M. Bao, G. Yuan, G. Xiao, T.A.O. Jin, Z. Li, X. Shu, Characteristics of TiNi thin films deposited by magnetron sputtering system with optical emission spectroscopy monitor, J. Surf Rev Lett 22 (2015), https://doi.org/10.1142/s0218625x15500638.

[36] N. Rodkate, M. Rutnakornpituk, Multi-responsive magnetic microsphere of poly(N-isopropylacrylamide)/carboxymethylchitosan hydrogel for drug controlled release, J. Carbohydr Polym 151 (2016) 251–259, https://doi.org/10.1016/j.carbpol.2016.05.081.

[37] W. Wei, X. Hu, X. Qi, H. Yu, Y. Liu, J. Li, J. Zhang, W. Dong, A novel thermo-responsive hydrogel based on salecan and poly(N-isopropylacrylamide): synthesis and characterization, J. Colloids Surf B Biointerfaces 125 (2015) 1–11, https://doi.org/10.1016/j.colsurfb.2014.10.057.

[38] X. Xu, Y. Liu, W. Fu, M. Yao, Z. Ding, J. Xuan, D. Li, S. Wang, Y. Xia, M. Cao, Poly(N-isopropylacrylamide)-based thermoresponsive composite hydrogels for biomedical applications, J. Polymers (Basel) 12 (2020), https://doi.org/10.3390/polym12030580.

[39] M. Cao, Y. Shen, Y. Wang, X. Wang, D. Li, Self-assembly of short elastin-like amphiphilic peptides: effects of temperature, molecular hydrophobicity and charge distribution, J. Molecules 24 (2019), https://doi.org/10.3390/molecules24010202.

[40] M.A. Haq, Y. Su, D. Wang, Mechanical properties of PNIPAM based hydrogels: a review, J. Mater Sci Eng C Mater Biol Appl 70 (2017) 842–855, https://doi.org/10.1016/j.msec.2016.09.081.

[41] S. Sarkar, T. Roy, A. Roy, S. Moitra, R. Ganguly, C.M. Megaridis, Revisiting the supplementary relationship of dynamic contact angles measured by sessile-droplet and captive-bubble methods: role of surface roughness, J. J Colloid Interface Sci 581 (2021) 690–697, https://doi.org/10.1016/j.jcis.2020.07.098.

[42] Y. Wang, X. Gong, Special oleophobic and hydrophilic surfaces: approaches, mechanisms, and applications, J. J Mater Chem A 5 (2017) 3759–3773, https://doi.org/10.1039/c6ta10474f.

[43] Y. Huang, J. Zhou, B. Su, L. Shi, J. Wang, S. Chen, L. Wang, J. Zi, Y. Song, L. Jiang, Colloidal photonic crystals with narrow stopbands assembled from low-adhesive superhydrophobic substrates, J. J Am Chem Soc 134 (2012) 17053–17058, https://doi.org/10.1021/ja304751k.

[44] L. Lin, M. Liu, L. Chen, P. Chen, J. Ma, D. Han, L. Jiang, Bio-inspired hierarchical macromolecule-nanoclay hydrogels for robust underwater superoleophobicity, J. Adv. Mater. 22 (2010) 4826–4830, https://doi.org/10.1002/adma.201002192.

[45] M.S. Bell, A. Borhan, A volume-corrected Wenzel model, J. Acs Omega 5 (2020) 8875–8884, https://doi.org/10.1021/acsomega.0c00495.

[46] Q. Cheng, M. Li, Y. Zheng, B. Su, S. Wang, L. Jiang, Janus interface materials: superhydrophobic air/solid interface and superoleophobic water/solid interface inspired by a lotus leaf, J. Soft Matter 7 (2011), https://doi.org/10.1039/c1sm05452j.

[47] X. Fan, F. Yang, J. Huang, Y. Yang, C. Nie, W. Zhao, L. Ma, C. Cheng, C. Zhao, R. Haag, Metal-organic-framework-derived 2D carbon nanosheets for localized multiple bacterial eradication and augmented anti-infective therapy, J. Nano Lett 19 (2019) 5885–5896, https://doi.org/10.1021/acs.nanolett.9b01400.

[48] D. Wilms, F. Schroer, T.J. Paul, S. Schmidt, Switchable Adhesion of *E. coli* to Thermosensitive carbohydrate-presenting microgel layers: a single-cell force spectroscopy study, J. Langmuir 36 (2020) 12555–12562, https://doi.org/10.1021/acs.langmuir.0c02040.

[49] C. Leng, H. Huang, K. Zhang, H.C. Hung, Y. Xu, Y. Li, S. Jiang, Z. Chen, Effect of surface hydration on antifouling properties of mixed charged polymers, J. Langmuir 34 (2018) 6538–6545, https://doi.org/10.1021/acs.langmuir.8b00768.

[50] C. Zhao, L. Zhou, M. Chiao, W. Yang, Antibacterial hydrogel coating: strategies in surface chemistry, J. Adv Colloid Interface Sci 285 (2020) 102280, https://doi.org/10.1016/j.cis.2020.102280.

[51] N. Datta, Q. Pham, U. Sharma, V. Sikavitsas, J. Jansen, A. Mikos, *In vitro* generated extracellular matrix and fluid shear stress synergistically enhance 3D osteoblastic differentiation, J. Proc Natl Acad Sci USA 103 (2006) 2488–2493, https://doi.org/10.1073/pnas.0505661103.

[52] Z. Yuan, B. Tao, Y. He, J. Liu, C. Lin, X. Shen, Y. Ding, Y. Yu, C. Mu, P. Liu, K. Cai, Biocompatible MoS_2/PDA-RGD coating on titanium implant with antibacterial property via intrinsic ROS-independent oxidative stress and NIR irradiation, J. Biomaterials 217 (2019), https://doi.org/10.1016/j.biomaterials.2019.119290, 119290.

[53] M. Sun, G. Chi, P. Li, S. Lv, J. Xu, Z. Xu, Y. Xia, Y. Tan, J. Xu, L. Li, Y. Li, Effects of matrix stiffness on the morphology, adhesion, proliferation and osteogenic differentiation of mesenchymal stem cells, J. Int J Med Sci 15 (2018) 257–268, https://doi.org/10.7150/ijms.21620.

[54] T.S. Dong, C.Y. Duan, S. Wang, X.Y. Gao, Q.Z. Yang, W.Z. Yang, Y. Deng, Multifunctional surface with enhanced angiogenesis for improving long-term osteogenic fixation of poly(ether ether ketone) implants, J. Acs Appl Mater Inter 12 (2020) 14971–14982, https://doi.org/10.1021/acsami.0c02304.

[55] L. Yu, S. Qian, Y. Qiao, X. Liu, Multifunctional Mn-containing titania coatings with enhanced corrosion resistance, osteogenesis and antibacterial activity, J. J Mater Chem B 2 (2014) 5397–5408, https://doi.org/10.1039/c4tb00594e.

[56] A.P. Kusumbe, S.K. Ramasamy, R.H. Adams, Coupling of angiogenesis and osteogenesis by a specific vessel subtype in bone, J. Nature 507 (2014) 323–328, https://doi.org/10.1038/nature13145.

[57] F.J. Zhao, B. Lei, X. Li, Y.F. Mo, R.X. Wang, D.F. Chen, X.F. Chen, Promoting *in vivo* early angiogenesis with sub-micrometer strontium-contained bioactive microspheres through modulating macrophage phenotypes, J. Biomaterials 178 (2018) 36–47, https://doi.org/10.1016/j.biomaterials.2018.06.004.

[58] J. Zhang, J. Pan, W. Jing, Motivating role of type H vessels in bone regeneration, J. Cell Prolif 53 (2020), e12874, https://doi.org/10.1111/cpr.12874.